The Cryosphere, 11, 191–215, 2017
www.the-cryosphere.net/11/191/2017/
doi:10.5194/tc-11-191-2017

The Cryosphere Open Access EGU

Diagnosing the decline in climatic mass balance of glaciers in Svalbard over 1957–2014

Torbjørn Ims Østby[1], Thomas Vikhamar Schuler[1], Jon Ove Hagen[1], Regine Hock[2,3], Jack Kohler[4], and Carleen H. Reijmer[5]

[1]Institute of Geoscience, University of Oslo, PO Box 1047 Blindern, 0316 Oslo, Norway
[2]Geophysical Institute, University of Alaska, Fairbanks, Alaska 99775-7320, USA
[3]Department of Earth Sciences, Uppsala University, Villavägen 16, 75236 Uppsala, Sweden
[4]Norwegian Polar Institute, Fram Centre, PO Box 6606 Langnes, 9296 Tromsø, Norway
[5]Institute for Marine and Atmospheric Research, Utrecht University, Princetonplein 5, 3584 CC Utrecht, the Netherlands

Correspondence to: Torbjørn Ims Østby (torbjorn.ostby@geo.uio.no)

Received: 8 July 2016 – Published in The Cryosphere Discuss.: 1 August 2016
Revised: 22 November 2016 – Accepted: 25 December 2016 – Published: 26 January 2017

Abstract. Estimating the long-term mass balance of the high-Arctic Svalbard archipelago is difficult due to the incomplete geodetic and direct glaciological measurements, both in space and time. To close these gaps, we use a coupled surface energy balance and snow pack model to analyse the mass changes of all Svalbard glaciers for the period 1957–2014. The model is forced by ERA-40 and ERA-Interim reanalysis data, downscaled to 1 km resolution. The model is validated using snow/firn temperature and density measurements, mass balance from stakes and ice cores, meteorological measurements, snow depths from radar profiles and remotely sensed surface albedo and skin temperatures. Overall model performance is good, but it varies regionally. Over the entire period the model yields a climatic mass balance of 8.2 cm w.e. yr^{-1}, which corresponds to a mass input of 175 Gt. Climatic mass balance has a linear trend of -1.4 ± 0.4 cm w.e. yr^{-2} with a shift from a positive to a negative regime around 1980. Modelled mass balance exhibits large interannual variability, which is controlled by summer temperatures and further amplified by the albedo feedback. For the recent period 2004–2013 climatic mass balance was -21 cm w.e. yr^{-1}, and accounting for frontal ablation estimated by Błaszczyk et al. (2009) yields a total Svalbard mass balance of -39 cm w.e. yr^{-1} for this 10-year period. In terms of eustatic sea level, this corresponds to a rise of 0.037 mm yr^{-1}.

Refreezing of water in snow and firn is substantial at 22 cm w.e. yr^{-1} or 26 % of total annual accumulation. However, as warming leads to reduced firn area over the period, refreezing decreases both absolutely and relative to the total accumulation. Negative mass balance and elevated equilibrium line altitudes (ELAs) resulted in massive reduction of the thick (> 2 m) firn extent and an increase in the superimposed ice, thin (< 2 m) firn and bare ice extents. Atmospheric warming also leads to a marked change in the thermal regime, with cooling of the glacier mid-elevation and warming in the ablation zone and upper firn areas. On the long-term, by removing the thermal barrier, this warming has implications for the vertical transfer of surface meltwater through the glacier and down to the base, influencing basal hydrology, sliding and thereby overall glacier motion.

1 Introduction

Glaciers are widely acknowledged as good indicators of climate change (e.g. AMAP, 2011), but the relationship between atmosphere, surface energy balance and glacier mass balance is complex. Glaciers and ice caps are currently among the major contributors to current sea level rise (Church et al., 2011), despite their relative small volume compared to the ice sheets of Greenland and Antarctica, and are assumed to be important throughout the 21st century (Meier et al., 2007). The high-Arctic archipelago Svalbard has an estimated total eustatic sea level rise potential of 17–26 mm (Martín-Español et al., 2015; Huss and Farinotti,

2012; Radić and Hock, 2010). Global glacier mass balance assessments suggest that Svalbard is one of the most important regional contributors to sea level rise over the 21st century, apart from Greenland and Antarctica (Giesen and Oerlemans, 2013; Marzeion et al., 2012; Radić et al., 2014), due to its location in one of the fastest-warming regions on Earth.

Through feedbacks in the climate system, the Arctic region experiences a greater warming than the global average, the so-called Arctic Amplification (e.g. Serreze and Francis, 2006). For the moderate emission scenario RCP4.5, Svalbard has a predicted warming of 5–8 °C and a precipitation increase of 20–40 % by 2100, relative to the period 1986–2005 (IPCC, 2013). Since the 1960s, there has been a strong warming of 0.5 °C decade^{-1} in Svalbard, the strongest warming measured in Europe (Nordli et al., 2014). Simultaneously there was a precipitation increase of 1.7 % decade^{-1} (Førland and Hanssen-Bauer, 2000). Steady negative glacier mass balance has been recorded since glaciological measurements began in 1967. However, direct measurements are mostly restricted to glaciers along the western coast of Svalbard, and are known to have more negative mass balance than the rest of the archipelago (Hagen et al., 2003a). Climatic mass balance (B_{clim}), the sum of surface mass balance and internal accumulation (Cogley et al., 2011), as derived from ice cores over 1960–2000 (Pinglot et al., 1999, 2001; Pohjola et al., 2002) and modelled balances for the period 1979–2013 (Lang et al., 2015a) show no trends. van Pelt et al. (2016) find a weakly positive precipitation trend, with the strongest changes observed to the north of the archipelago. In contrast, geodetic mass balance studies indicate accelerated glacier mass loss over the last decades (James et al., 2012; Kohler et al., 2007; Nuth et al., 2010). There are multiple causes for this apparent disagreement. Geodetic approaches include all components of the mass budget, i.e. the climatic balance and mass losses through calving and submarine melting at tidewater glacier termini. In addition, ice cores are taken in the accumulation area, while trends in the ablation area may differ; the latter have been shown to have a substantial effect on the glacier-wide climatic balances in Svalbard (e.g. Aas et al., 2016; van Pelt et al., 2012). Meteorologically driven mass balance modelling facilitates filling in these spatial and temporal gaps; however care must be taken to adequately represent spatial and temporal scales of relevant processes. For instance, the coarse spatial 10 km grid used by Lang et al. (2015a) does not represent the glacier hypsometry at lower elevations well, thereby influencing the results.

Here we present results from a model study that covers the entire archipelago for the period 1957–2014 at high spatial and temporal resolution. At time steps of 6 h, we calculate the mass and energy fluxes at the glacier surface and in the subsurface layers using the model DEBAM (Distributed Energy Balance Model) developed by Hock and Holmgren (2005) and Reijmer and Hock (2008). We downscale ERA-40 (Uppala et al., 2005) and ERA-Interim (Dee et al., 2011) climate reanalysis data to 1 km horizontal resolution, largely following the TopoSCALE methodology (Fiddes and Gruber, 2014), except for precipitation, where we use the linear theory (LT) for orographic enhancement (Smith and Barstad, 2004). We conduct a thorough comparison with a large number and different types of observations to validate model performance. From our model results we identify climatic controls on the climatic mass balance over the study period and discuss implications for the future by testing sensitivities and applying perturbations representing a 2100 climate as suggested by Førland et al. (2011). We also examine modelled responses of the water retention capacity in a warmer climate and discuss related implications for B_{clim} and ice dynamics through changes in the hydrological and thermal regimes.

2 Svalbard climate and target glaciers

The Svalbard archipelago is located in the Norwegian Arctic between 75 and 81° N (Fig. 1). The land area of the islands is $\sim 60\,000\,\mathrm{km}^2$ of which 57 % is covered by glaciers (Nuth et al., 2013). While the western side of the archipelago is characterized by alpine topography, the eastern side has less rugged topography and many low-altitude ice caps.

Through the Norwegian current, an extension of the Gulf stream, warm Atlantic water is advected northwards keeping the western side of Svalbard mostly ice-free year-round (Walczowski and Piechura, 2011). In contrast, the ocean east of Svalbard is dominated by Arctic ocean currents (Loeng, 1991). Similarly, contrasting regimes are found in the atmosphere, where warm and moist air is associated with southerly flow, while colder and drier air masses originate in the north-east (Kaesmacher and Schneider, 2011). These oceanic and atmospheric circulation patterns combined with the fluctuating sea ice edge cause large temporal and spatial gradients of temperature and precipitation across the archipelago (Hisdal, 1998). Therefore, Svalbard has been identified as one of the most climatically sensitive regions in the world (Rogers et al., 2005).

The climate of Svalbard is polar maritime, with both rain or snowfall possible in all months of the year. At the main settlement Longyearbyen, mean annual air temperature for the normal period 1961–1990 is −6.7 °C. A warming trend of 2.6 °C century^{-1} has been identified from the 117-year-long Svalbard Airport temperature record (Nordli et al., 2014); Supplement (Figs. S1–S2). Although a positive trend exists for all seasons, the annual trend is dominated by an increase in winter temperatures. Increased air temperatures and precipitation have occurred simultaneously with reduced sea ice cover around Svalbard (Rodrigues, 2008).

Annual precipitation in Longyearbyen is 190 mm and has increased by 2.5 % decade^{-1} over the last 80 years (Førland et al., 1997; Hanssen-Bauer and Førland, 1998), although precipitation gauge undercatch complicate trend analysis (Førland et al., 1997; Hanssen-Bauer and Førland, 1998; Førland and Hanssen-Bauer, 2003). Large precipitation vari-

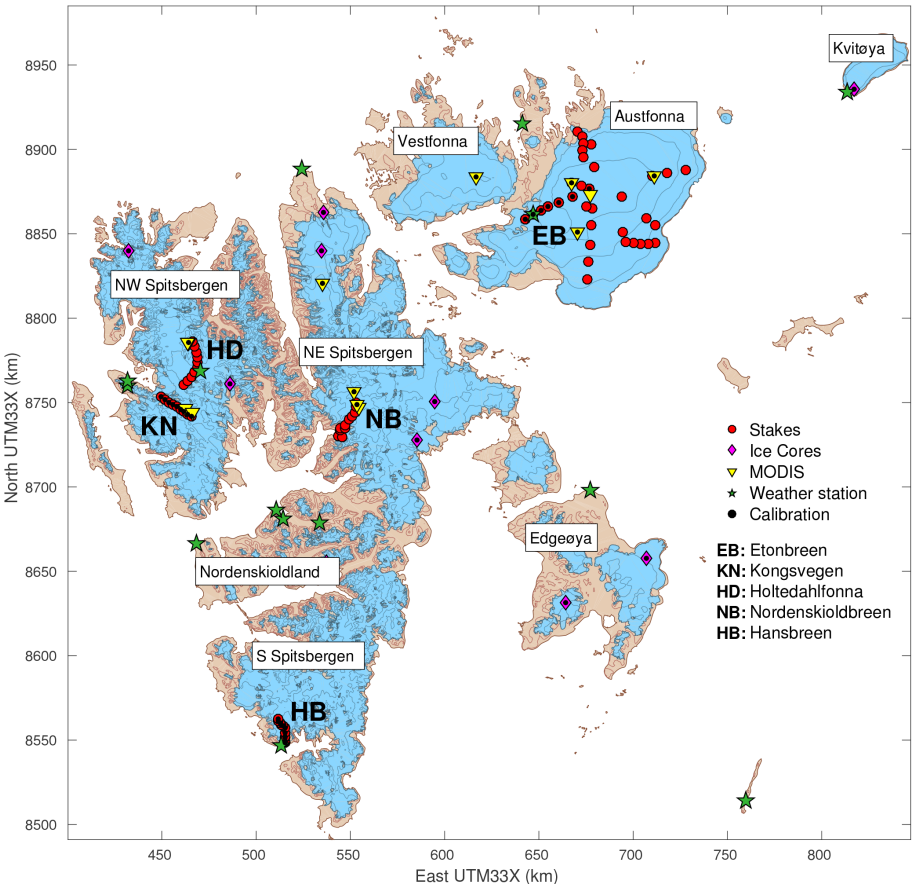

Figure 1. Map of Svalbard with names of regions and the five glaciers described in the text; glacierized area is shown in blue. Markers show the locations of observations and the black dots mark the calibration sites. Lines mark elevation above sea level in 200 m intervals.

ability is observed across the archipelago, with precipitation about three times higher along the west coast compared to Longyearbyen (Førland and Hanssen-Bauer, 2003) and even more in southern Spitsbergen (Sand et al., 2003; Winther et al., 2003). The drier central Spitsbergen has less extensive glacier coverage and is characterized by land-terminating cirque and valley glaciers.

Surface mass balance is measured at stakes along the centre profiles of five glaciers (see Fig. 1). Etonbreen ($\sim 640\,\mathrm{km}^2$) is the largest of these glaciers, and drains gently westwards from the summit of the Austfonna ice cap. Surface mass balance has been monitored at Austfonna since 2004, but the stakes along Etonbreen are the only ones which have been measured every year. Glacier-wide-specific surface mass balance has been close to zero, but margin retreat since the last surge in the 1930s makes the overall mass balance negative. Kongsvegen ($\sim 100\,\mathrm{km}^2$) and Holtedahlfonna ($\sim 385\,\mathrm{km}^2$) are situated in north-western Spitsbergen with mass balances measurements since 1987 and 2003 respectively. The ice field Holtedahlfonna feeds Kronebreen, a steady fast-flowing glacier, while Kongsvegen is nearly stagnant, since it is in the quiescent phase after a surge in 1948 (Kääb et al., 2005). Kongsvegen and Kronebreen merge downstream and enter Kongsfjorden together. Despite the proximity the two glaciers, Kongsvegen has higher specific accumulation rates than Holtedahlfonna, but because of their distinct hypsometries, glacier-wide surface mass balance on Kongsvegen ($-4\,\mathrm{cm\,w.e.\,yr}^{-1}$) is slightly more negative than Holtedahlfonna ($-2\,\mathrm{cm\,w.e.\,yr}^{-1}$) over 1966–2007 (Nuth et al., 2012). However, calving and marginal retreat of Kronebreen make the overall mass balance of the combined Kronebreen and Holtedahlfonna system strongly negative. Nordenskiöldbreen ($\sim 200\,\mathrm{km}^2$) is a valley glacier located in central Spitsbergen, flowing south-west from the Lomonosovfonna ice field into the Adolfbukta fjord. Mass balance has been measured since 2006 and is negative (van Pelt et al., 2012). Hansbreen ($\sim 56\,\mathrm{km}^2$) is a marine-terminating glacier, where mass balance has been measured since 1989. Surface mass balance has been negative by $-28\,\mathrm{cm\,w.e.\,yr}^{-1}$ since 1989, and wind redistribution of snow is important on Hansbreen (Grabiec et al., 2006, 2012).

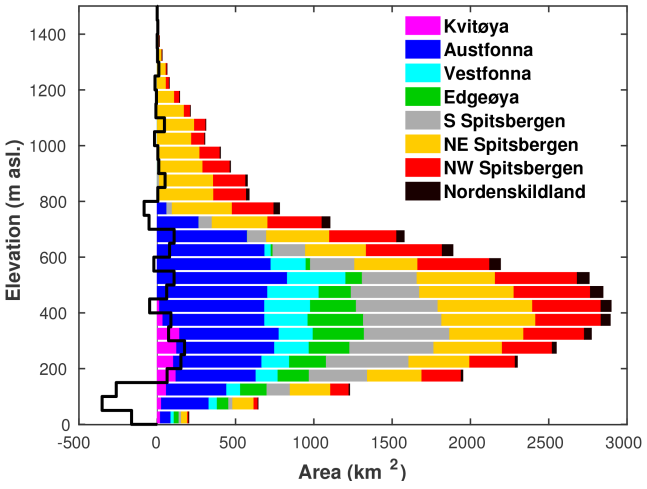

Figure 2. Regional glacier hypsometry of the 2000s inventory. Stacked bars correspond to the entire Svalbard glacier area. Altitude intervals of 50 m. The black line is the difference between hypsometry of the 90 m DEM and the applied 1 km DEM, for the whole of Svalbard.

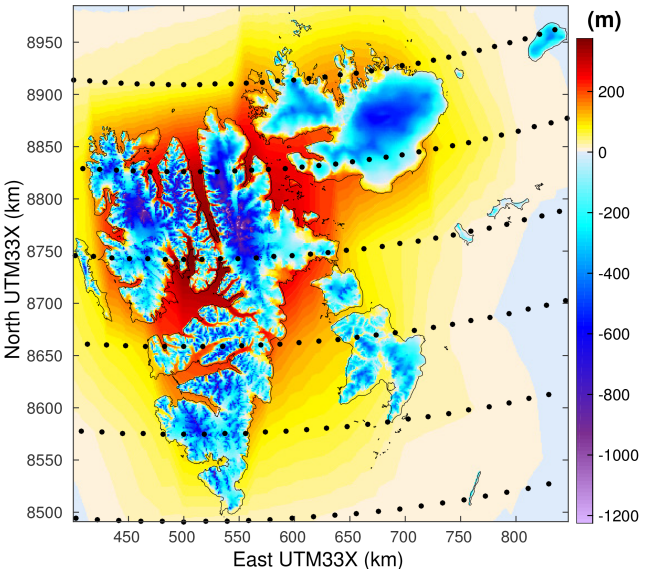

Figure 3. Elevation difference (m) between the ERA topography and the 1 km DEM; negative values mean that ERA elevations are lower. Black dots show the 0.75° × 0.75° ERA grid.

3 Data

3.1 Topography and glacier masks

The 1 km resolution digital elevation model (DEM) used in this study was resampled from a 90 m DEM by Nuth et al. (2010). Slope and aspect were computed following Zevenbergen and Thorne (1987). Fractional glacier masks were created by computing the percentage of glacier coverage for each grid point of the 1 km DEM for three periods (1930–1960s, 1990s and 2000s) based on a multi-temporal inventory (Nuth et al., 2013; Arendt et al., 2015). However, only the latest DEM has a complete coverage over all of Svalbard (Fig. S3). We created a fourth fractional glacier mask that combines the masks from the three periods so that each grid cell contains the largest glacier extent of any of these periods (henceforth referred to as the reference glacier mask). Finally, an annual time series of glacier masks was created by linear interpolation, thus assuming linear glacier retreat or advance between the epochs and no changes after the 2000s epoch (Fig. S4).

Small discrepancies are introduced by converting glacier polygons to the 1 km grid. While the glacier cover in the 2000s inventory is 33 775 km^2 the fractional glacier mask is 14 km^2 (0.04 %) larger. The reference glacier mask covers 36 943 km^2 and is 10 % larger than the 2000s inventory. Figure 2 shows the hypsometry of the glacierized area of each region and of all Svalbard regions combined. The error (area difference in each elevation bin between 90 m and 1 km DEM) is generally low, but glacier area in the 1 km DEM is slightly underestimated below 150 m a.s.l.

3.2 Downscaled ERA-40 and ERA-Interim climate reanalysis data

The glacier model is forced by fields of downscaled near-surface air temperature, relative humidity, wind and downwelling shortwave and longwave radiation from the ERA-40 and ERA-Interim reanalyses of the European Centre for Medium-Range Weather Forecasts (Uppala et al., 2005; Dee et al., 2011). The reanalysis data are provided at 6 h intervals on a 0.75° × 0.75° spatial grid (Fig. 3), covering the periods 1957–2002 (ERA-40) and 1979–2014 (ERA-Interim). We use downscaled variables from ERA-40 for the period 1957–1978 and ERA-Interim from 1979 onwards. To investigate the potential effects of this heterogeneity in our composite forcing, we have evaluated both data sets for the overlap period 1979–2002 at a number of points (Fig. 1).

Precipitation is often heavily biased in coarsely resolved reanalyses, especially in environments with pronounced topography, where it is typically too low and lacks spatial detail (Schuler et al., 2008). This is associated with the smoothed representation of the actual topography in the large-scale model used for the reanalysis (Fig. 3), leading to an underestimate of orographic precipitation enhancement. We assume that this is the main reason for the poor performance of reanalysed precipitation, and instead use a linear theory (LT) of orographic precipitation (Smith and Barstad, 2004) to account for orographic enhancement when downscaling ERA-precipitation to our 1 km resolution model domain. The LT model describes the motion of an air parcel, characterized by its temperature, stability, wind direction and speed. Terrain-induced uplift of the air parcel results in condensation and

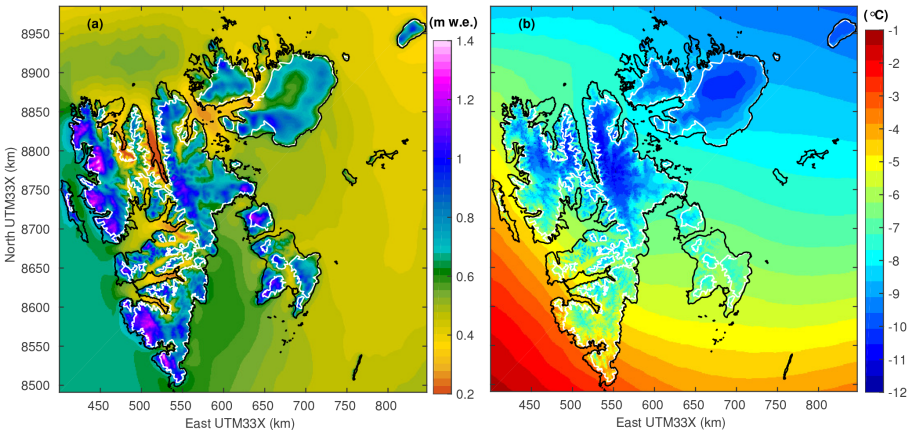

Figure 4. Downscaled annual precipitation **(a)** and annual mean 2 m air temperature **(b)** averaged over the ERA-Interim period 1979–2014.

eventually precipitation of moisture further downstream of the uplift. This model has been successfully evaluated using precipitation gauges (Barstad and Smith, 2005) and snow measurements (Schuler et al., 2008) and applied for downscaling precipitation (e.g. Crochet et al., 2007). To discriminate solid from liquid precipitation, a simple thresholding approach was used, assuming that all precipitation is liquid at temperatures above 2.5 °C and solid at temperatures below 0.5 °C, with a linear transition in between.

The other required climate variables are downscaled to the 1 km grid using the TopoSCALE methodology (Fiddes and Gruber, 2014). TopoSCALE exploits the relatively high vertical resolution of the reanalysis data, since downscaled variables at the actual topography are based on the properties of the vertical structure in the reanalysis. The downscaled fields preserve the horizontal gradients present in ERA, but include additional features caused by the real topography not present in ERA (Fig. 4). This approach is assumed to outperform simpler bias corrections, since transient properties of the atmosphere are accounted for. For example, transient lapse rates including inversions in the reanalysis data will be preserved in the downscaled product.

We modify the TopoSCALE methodology regarding downscaling of direct shortwave radiation and air temperature. For direct solar radiation we apply the relationship in Kumar et al. (1997) to atmospheric attenuation rather than the one given in Fiddes and Gruber (2014). Solar geometry variables such as solar zenith and azimuth, and topographic shading due to local slope and aspect are calculated following Reda and Andreas (2004). Cast shadow and hemispherical obstructions caused by surrounding topography are calculated following Ratti (2001).

During summer when air temperatures (T_{air}) are above freezing, the TopoSCALE method resulted in too-high (low) T_{air} values wherever the actual topography is above (below) the ERA topography. During summer, surface temperatures are restricted to the melting point, even as air temperatures aloft are warmer. This near-surface inversion gives rise to erroneous extrapolation when used to scale temperatures over a large vertical distance. To avoid this problem, we use ERA 2 m T_{air} in the downscaling under these conditions, implying that vertical lapse rates vanish whenever melt occurred in the reanalysis.

3.2.1 Validation of climate input

Downscaled variables are compared to observations at the meteorological stations listed in Table 1, mostly for the period after 2004. Daily averages of air temperature, relative humidity, wind speed and radiation and monthly precipitation of the closest model grid point are compared to the corresponding variable at the measuring site. Air temperature (2 m) is by far the most commonly measured variable, while radiation components are available only at two stations (Table 1). Despite altitude differences of up to 100 m, between the measuring site and the corresponding cell in the model, no altitude correction is performed due to unknown lapse rates.

In general the agreement is good between downscaled ERA and observed air temperatures, with biases mostly below 1.5 K (Table 2). Despite a small bias for mean annual temperatures, there is a clear seasonal bias, with ERA temperatures too warm during winter and too cold during summer (Fig. 5). Although the biases in Fig. 5 are negative during summer, ERA is too warm over the glaciers during summer, when 2 m air temperatures are above freezing.

At Svalbard Airport, the performances of downscaled ERA-40 and ERA-Interim are investigated for the entire model period. Over 1957–1979 only monthly measured temperatures are available at Svalbard Airport, where downscaled ERA-40 has a monthly root mean square error (RMSE) of 2.3 °C. For the 1979–2002 period the reanalysis products overlap with a monthly RMSE of 1.8 and 1.5 °C at Svalbard Airport for ERA-40 and ERA-Interim respectively. We attribute the lower performance prior to 1979 to the lack

Table 1. Meteorological stations used for validation of the downscaled ERA-Interim reanalysis. N indicates the number of daily averages used in the validation, subscript T refers to 2 m air temperature, RH is relative humidity, ws is wind speed, L and S is downwelling short- and longwave radiation and prec is precipitation. Also given is the elevation of the observation site (Z) and the closest grid point (Z_{DEM}).

Location	Long.	Lat.	Z (m a.s.l.)	Z_{DEM} (m a.s.l.)	Period	N_T	N_{RH}	N_{ws}	$N_{S,L}$	N_{prec}
Etonbreen[2]	22.42	79.73	369	350	2004–d.d.	3295	2738	2913	3240	0
Janssonhaugen	16.47	78.18	270	163	2011–d.d.	910	0	945	0	0
Gruvefjellet	15.62	78.20	464	359	2007–d.d.	2555	2555	2551	0	0
Kapp Heuglin	22.82	78.25	18	4	2006–d.d.	2099	0	2112	0	0
Rijpfjorden	22.48	80.22	10	31	2007–d.d.	1495	1495	1304	0	0
Svalbard Airport	15.47	78.25	28	3	1976–d.d.	12 777	0	12 724	0	199[1]
Isfjord Radio	13.63	78.07	13	1	2000–2006	1666	0	0	0	0
Verlegenhuken	16.25	80.06	8	0	2011–d.d.	986	0	1700	0	0
Hornsund	15.54	77.00	10	8	1996–d.d.	4635	0	4473	0	95[1]
Kvitøya	31.50	80.07	10	17	2012–d.d.	740	0	702	0	0
Holtedahlfonna[2]	13.62	78.98	688	702	2009–2010	317	0	265	0	0
Ny-Ålesund	11.93	78.92	8	6	1975–d.d.	12 666	12 708	12 349	0	212[1]
Bayelva	11.83	78.92	25	28	2003–d.d.	3652	0	0	3652	0
Hopen	25.01	76.51	6	60	1957–d.d.	13 178	0	13 044	0	306[1]

[1] Number of months. [2] Station located on glacier.

of satellite observations available for constraining sea surface temperatures and sea ice cover in the reanalysis. Since the temperature records of Svalbard Airport and other sites on the west coast are likely to be incorporated into the reanalysis, the quality of the reanalysis in the pre-satellite era is possibly even lower in remote areas with no observations. The annual observed air temperature trend for the period 1957–2013 at Svalbard Airport is $0.70 \pm 0.22\,^{\circ}\mathrm{C\,decade^{-1}}$, while the downscaled ERA data have an insignificantly lower warming trend of $0.67 \pm 0.19\,^{\circ}\mathrm{C\,decade^{-1}}$ at Svalbard Airport.

Downwelling shortwave and longwave radiation are compared to measurements at Etonbreen (Schuler et al., 2014) and the Baseline Surface Radiation Network site in Ny-Ålesund (Maturilli et al., 2013). In Ny-Ålesund the model largely reproduces observations both for short and longwave radiation. During winter, downwelling longwave radiation is slightly underestimated, while there is no bias during summer. Since there is no temperature bias in Ny-Ålesund during winter, the underestimation of longwave radiation is indicative of a too-thin cloud cover in the reanalysis. Representations of clouds are among the major issues of the reanalysis (Aas et al., 2016). Downwelling shortwave radiation is overestimated by $7\,\mathrm{W\,m^{-2}}$ over the summer season in Ny-Ålesund. There is a much better agreement with radiation observations in Ny-Ålesund than in north-eastern Svalbard. This is to be expected, since radio soundings and other observation data from Ny-Ålesund are assimilated into ERA-Interim. Therefore, cloud cover at Ny-Ålesund is much better represented by the reanalysis than at Austfonna.

On Etonbreen during summer, downwelling shortwave radiation is underestimated by $40\,\mathrm{W\,m^{-2}}$ while downwelling longwave radiation is overestimated by $12\,\mathrm{W\,m^{-2}}$, indicative

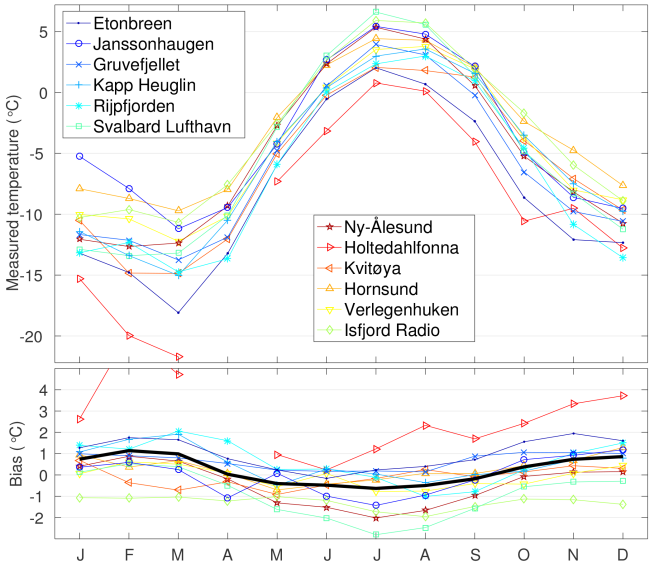

Figure 5. Observed monthly mean 2 m air temperatures (upper panel) and biases given by downscaled minus observational monthly averages (lower panel). Bold black line is the average over the 12 sites.

of a too-thick atmosphere or too many clouds in the reanalysis. However, these biases could be partly explained by measurement uncertainty caused by rime on the sensor or by sensor tilt. The latter issue is caused by melt and deformation of the foundation of the autonomous weather stations causing sensor tilt, changed hemispherical view and thereby errors, especially at large solar zenith angles (Bogren et al., 2016).

Wind speeds are reproduced reasonably well, including in the seasonal cycle. Biases are within $\pm 1.5\,\mathrm{m\,s^{-1}}$ with no

clear seasonal trend. It is likely that the biases are caused by site-specific effects, such as the deceleration of airflow in the lee of a topographic obstacle or acceleration due to being channelized through valleys.

For relative humidity the reanalysis represents the seasonality well, and in late summer both the humidity and the biases are at their largest magnitudes. At the two coastal stations at Hopen and Rijpfjorden, the downscaled reanalysis is too dry, whereas it is too humid at the two higher elevation stations. The coarse land mask of the reanalysis and the poor representation of sea ice are most likely the main causes for these biases.

Downscaled precipitation is overestimated by 5 to 25 mm per month at the weather stations, with a slightly higher bias during winter. These biases are partly caused by measurement undercatch, which is reported to be 50 % at Svalbard on an annual basis, with higher undercatch during winter than during summer (Førland and Hanssen-Bauer, 2000).

3.3 Satellite-derived surface temperatures and albedo

3.3.1 MODIS skin surface temperatures

Skin surface temperatures (T_{surf}) derived from the Moderate Resolution Imaging Spectroradiometer instruments (MODIS) on board the Terra and Aqua satellites are used to constrain modelled surface temperatures. We use the MODIS level 3 collection 5 products MOD11A1 (Terra) and MYD11A1 (Aqua), the surface temperatures of which are retrieved using the split-window algorithm (Wan and Dozier, 1996; Wan, 2008). Cloudy satellite scenes are masked out using the MODIS cloud mask products MOD35_L2 and MYD35_L2 (Ackerman et al., 1998; Frey et al., 2008). Under cloud-free conditions Terra and Aqua combined provide four estimates of T_{surf} per day at 1000 m resolution. Automatically generated quality control flags represent the confidence level of the produced T_{surf}. As suggested by Østby et al. (2014), observations flagged as "other quality" and "T_{surf} error < 3" have been excluded. MODIS T_{surf} usually has an accuracy better than 1 K (Wan, 2014). However, a much lower accuracy is found for snow and ice surfaces due to the ambiguous cloud detection caused by the spectral similarities of snow and clouds (Hall et al., 2004, 2008; Scambos et al., 2006; Østby et al., 2014). For Svalbard Østby et al. (2014) found an RMSE $= 5.0$ K and bias of -3.0 K. Figure S5 in the Supplement show average T_{surf} and minimum albedo from MODIS.

3.3.2 MODIS albedo

Similar to the MODIS surface temperatures, daily satellite-derived albedo is provided by the snow cover products MOD10A1 and MYD10A1, at 500 m spatial resolution (Hall and Riggs, 2007). To minimize possible errors in the satellite albedo, acquisition during days of noon solar zenith above 70° were excluded (Schaaf et al., 2011). Mean daily albedo was only calculated if both Terra and Aqua had observations flagged as "good" by the internal quality check. Observations were also discarded if the albedo difference between Aqua and Terra exceeded 0.1, since such rapid and large albedo change can only occur during snowfall, when clouds should still preclude acquisition as they are opaque in the visible and thermal regions of the spectrum. Given these criteria, the satellite-derived albedo yielded RMSE $= 0.08$, mean bias $= -0.005$ and $R^2 = 0.72$ compared to the noontime albedo measured at Etonbreen.

4 Model description

A surface energy balance model coupled to a snow pack model was used to calculate surface energy fluxes, mass balance, water retention and snow and ice properties. Only the main features will be described here; details can be found in Reijmer and Hock (2008); Hock and Holmgren (2005); Østby et al. (2013). Our model set-up employs slightly different parameterizations for albedo, thermal conductivity and run-off, compared to the original model.

4.1 Surface energy balance

The energy balance at the glacier surface is given by

$$Q_{\mathrm{N}} + Q_{\mathrm{H}} + Q_{\mathrm{L}} + Q_{\mathrm{R}} + Q_{\mathrm{G}} + Q_{\mathrm{M}} = 0, \quad (1)$$

where net radiation is $Q_{\mathrm{N}} = S_{\downarrow}(1-\alpha) + L_{\downarrow} + L_{\uparrow}$. Downwelling short and longwave radiation fluxes are taken from downscaled ERA reanalysis data. Turbulent fluxes of sensible heat (Q_{H}) and latent heat (Q_{L}) are calculated from the Monin–Obukhov theory using downscaled humidity, wind speed and air temperatures at screen level (2 m). Roughness lengths of momentum for snow and ice surfaces are determined through calibration (Sect. 4.4), while roughness lengths for heat and vapour are calculated according to Andreas (1987). Sensible heat supplied by rain water (Q_{R}) is derived from the rainfall rate, assuming that the hydrometeors have the same temperature as the surrounding air. Q_{G} is the energy exchange with the subsurface layer (Sect. 4.2). Q_{M} is the energy flux used for melting snow and ice. The sign convention is such that fluxes directed towards the surface carry a positive sign and vice versa.

Albedo

Since shortwave radiation is generally the most important energy supply for melt on Arctic glaciers (e.g. Arendt, 1999; Arnold et al., 2006; Østby et al., 2013), we carefully constructed an albedo parameterization similar to the one by Bougamont and Bamber (2005). Albedo is set to a maximum value during snowfall. Snow ageing induces exponential albedo decay with different temperature dependent

Table 2. Seasonal biases in meteorological variables (downscaled minus observational averages) at all observation sites averaged over each site's observation period (Table 1). Shown are air temperature T, relative humidity, RH, wind speed, WS, shortwave radiation, $S_{\downarrow}$, longwave radiation, $L_{\downarrow}$ and precipitation, P. Column headings S and W denote summer (June–August) and winter (September–May) respectively. Positive numbers indicate that the model results are larger than the observations. The second row at each site (italicized font) shows the bias between the downscaled and corresponding coarse ERA variable.

Location	ΔT (K)		ΔRH (%)		ΔWS ($m s^{-1}$)		$\Delta S_{\downarrow}$ ($W m^{-2}$)		$\Delta L_{\downarrow}$ ($W m^{-2}$)		ΔP (mm)	
	S	W	S	W	S	W	S	W	S	W	S	W
Etonbreen	0.2	1.3	−2.2	−5.4	0.3	0.2	−40	−10	12	−14	–	–
	1.1	*1.9*	*−2.2*	*−5.4*	*0.3*	*0.2*	*−37*	*−9*	*17*	*−16*	–	–
Janssonhaugen	−1.1	0.3	–	–	−1.8	−1.3	–	–	–	–	–	–
	−1.0	*−0.6*	–	–	*−1.8*	*−1.3*	–	–	–	–	–	–
Gruvefjellet	0.2	0.8	3.1	−2.9	0.0	−0.2	–	–	–	–	–	–
	0.7	*0.9*	*3.1*	*−2.9*	*0.0*	*−0.2*	–	–	–	–	–	–
Kapp Heuglin	−0.0	0.7	–	–	−0.0	1.0	–	–	–	–	–	–
	0.3	*1.0*	–	–	*−0.0*	*1.0*	–	–	–	–	–	–
Rijpfjorden	−0.3	0.9	5.7	2.6	0.8	0.9	–	–	–	–	–	–
	0.0	*0.6*	*5.7*	*2.6*	*0.8*	*0.9*	–	–	–	–	–	–
Svalbard Airport	−2.4	−0.4	–	–	−1.3	−1.0	–	–	–	–	25	26
	−2.4	*−2.2*	–	–	*−1.3*	*−1.0*	–	–	–	–	–	–
Isfjord Radio	−1.6	−1.2	–	–	–	–	–	–	–	–	–	–
	−1.5	*−0.5*	–	–	–	–	–	–	–	–	–	–
Verlegenhuken	−0.5	0.0	–	–	−1.9	−1.7	–	–	–	–	–	–
	−0.3	*0.5*	–	–	*−1.9*	*−1.7*	–	–	–	–	–	–
Hornsund	−0.2	0.4	–	–	−0.0	0.4	–	–	–	–	5	19
	−0.0	*0.8*	–	–	*−0.0*	*0.4*	–	–	–	–	–	–
Kvitøya	−0.1	−0.1	–	–	−0.9	−1.3	–	–	–	–	–	–
	0.3	*0.6*	–	–	*−0.9*	*−1.3*	–	–	–	–	–	–
Holtedahlfonna	1.3	–	–	–	−0.7	–	–	–	–	–	–	–
	3.2	–	–	–	*−0.7*	–	–	–	–	–	–	–
Ny-Ålesund	−1.7	−0.0	7.6	3.2	0.7	0.8	−7	4	2	9	23	18
	−1.6	*−1.2*	*7.6*	*3.2*	*0.7*	*0.8*	*−8*	*3*	*0*	*15*	–	–
Hopen	1.9	5.2	–	–	0.3	−0.1	–	–	–	–	7	10
Bayelva	2.1	−0.0	–	–	–	–	–	–	–	–	–	–

timescales for wet and dry snow. In case of a thin snow cover, albedo is reduced from snow albedo to the underlying albedo (firn, ice or superimposed ice), using the relationship described by Oerlemans and Knap (1998), with a characteristic snow-depth scale of 3 cm, such that the albedo transition is smooth when snow cover is thin. Precipitation events are frequent (∼ 200 days a year), but usually yield low amounts (Aleksandrov et al., 2005). The snow-depth dependency is essential to avoid the snow albedo being reset to fresh snow albedo in case of an insignificantly thin fresh snow layer. A similar approach was used for albedo reduction to account for water ponding at the surface with a characteristic water depth of 30 cm (Zuo and Oerlemans, 1996). Threshold values for albedo of firn and ice are determined during calibration (Sect. 4.4). Finally, albedo is adjusted for specular reflection at large zenith angles following Gardner and Sharp (2010).

4.2 Subsurface processes

The subsurface model is based on the SOMARS model (Simulation Of glacier surface Mass balance And Related Subsurface processes Greuell and Konzelmann, 1994), which calculates temperature, density and water content of the subsurface layers and the subsurface energy flux Q_G. The surface energy balance and subsurface model are connected through the skin surface temperature, assuming the surface to be an infinite layer with zero heat capacity. Percolation follows a tipping-bucket scheme, wherein water percolating downwards is partly retained by capillary forces or refreezes upon encountering layers at sub-zero temperatures. When water meets impermeable ice, slush builds up and lateral run-off is computed using relationships defined by Zuo and Oerlemans (1996). A density-dependent thermal conductivity parameterization (Douville et al., 1995) was calibrated for computing subsurface heat conduction. Irreducible water content is calculated after Schneider and Jansson (2004) and densification of dry snow after Herron and Langway (1980).

4.3 Climatic mass balance

The climatic mass balance is the sum of melt and (re-)sublimation at the surface, refreezing in the subsurface layers and solid precipitation from the downscaled reanalysis. Although the model also calculates the water balance, liquid water retained in snow or firn is not included in the mass balance (Cogley et al., 2011).

4.4 Model set-up and calibration

The model is run for each glacierized grid cell based on the reference glacier mask (Sect. 3.1). The temporal resolution of the surface energy balance is that of the ERA reanalysis (6 h), while the snow model uses an internal time step of 3 min for which the ERA forcing is linearly interpolated. The subsurface model is solved on an adaptive grid consisting of 15–35 layers, with a maximum depth of ~ 40 m below the surface. Layers close to the surface are few centimetres thick, while the layers closer to the bottom are several metres thick.

Snow/ice temperature, density and water content are initialized with a 10-year spin-up using the climate data of the 1960s. To start the spin-up, the entire subsurface domain has an initial density of ice (900 kg m^{-3}), zero water content and temperatures of 0 °C at the surface; the latter linearly decrease to −5 °C at 7 m depth, beyond which the temperature remains constant. The initial value of −5 °C at depth is somewhat higher than the mean annual air temperature, and is based on observed temperatures in boreholes (Björnsson et al., 1996). Different initial conditions for the spin-up period had little effect on the results at most locations where the spin-up time was tested. A few exceptions occurred at some locations close to the equilibrium line, where system memory seems to be longer; at these locations differences in annual mass balance of up to 5 cm w.e. yr^{-1} occurred in the first years following the spin-up period, when a 10-year spin-up is run twice instead of once.

Since model calibration is computationally expensive, only 48 grid cells were selected for calibration. Most of these sites correspond to locations where mass balance is monitored, but additional sites were included to achieve a good spatial coverage over the entire archipelago (Fig. 1). At these additional sites only remote sensing data were available for calibration. Glacier edges were avoided such that the MODIS data (1 and 0.5 km resolution) were entirely on glaciers when resampled to the applied 1 km DEM.

Even though the model is physically based, some parameters do not have a consensus estimate in the literature. Østby et al. (2014) showed that model performance is sensitive to the choice of parameters concerning the turbulent fluxes (roughness lengths) and the albedo parameterization. Here, the model is calibrated using an adaptive Markov Chain Monte Carlo solver entitled DREAM$_{ZS}$ (Differential Evolution Adaptive Metropolis) (Vrugt et al., 2009; Laloy and Vrugt, 2012). This approach enables parallel computing, since the Markov chains evolve almost separately. Four parameters were selected for calibration: roughness lengths for snow and ice surfaces, and albedo for firn and ice. DREAM$_{ZS}$ seeks to maximize the likelihood L of an observed quantity (O) and its corresponding quantity predicted by the model (P) using

$$L = \frac{-N\,\ln(2\pi)}{2} - \sum_{i}^{N} \ln(\sigma_i) - \frac{\left(\sum_i^N \left(\frac{P_i - O_i}{\sigma}\right)^2\right)}{2}, \qquad (2)$$

where N is the number of samples and σ is the uncertainty of the measurement.

Table 3. Data used for calibration: point annual (b_a), summer (b_s), winter (b_w) mass balances, albedo (α), surface temperature from MODIS ($T_{s,\,MODIS}$), longwave outgoing radiation ($L_{\uparrow,AWS}$) and surface-height changes (SR_{AWS}) from a sonic ranger. Subscript AWS indicates that data are from the automatic weather station at Etonbreen. $T_{i,AWS}$ is snow and ice temperatures measured by a thermistor string next to the Etonbreen AWS. Sites indicate the number of sites for which each of the listed data variables are available, N is the total number of observations, and σ is the assumed observation uncertainty.

Data (unit)	Sites	N	σ
b_a (cm w.e.)	30	268	10
b_s (cm w.e.)	30	259	10
b_w (cm w.e.)	30	294	10
α_{MODIS} (%)	48	9386	8
$T_{s,\,MODIS}$ (K)	48	315 615	5
α_{AWS} (%)	1	1424	4
$L_{\uparrow,AWS}$ (W m^{-2})	1	10 826	3
SR_{AWS} (cm)	1	10 384	3
$T_{i,AWS}$ (K)	1	33 222	0.25

Nine different types of data are used for calibration. Table 3 lists the variables along with the measurement uncertainty σ and number of observations N. Uncertainty of stake mass balance is assumed to be 10 cm w.e., in the lower range of reported uncertainties (e.g. Huss et al., 2009; Zemp et al., 2013). We adopt this low value due to the low mass turnover in Svalbard, but acknowledge that higher uncertainties are likely for the accumulation area. For MODIS-derived albedo we apply an uncertainty of 8 % (Sect. 3) and 5 K for MODIS T_{surf} (Østby et al., 2014). For the measurements at the automatic weather station we assume $\sigma = 3$ W m^{-2} for longwave radiation (Michel et al., 2008), while uncertainties for the albedo, the sonic ranger data and snow and ice temperatures from the thermistor string are provided by the instrument manufacturers (Schuler et al., 2014; Østby et al., 2013).

Likelihood functions for each of the nine data types are summed and the parameter set yielding the highest total L is applied in the simulations. Calibrated parameter values and other model parameters are listed in Table S1.

Table 4. Climatic mass balance components in cm w.e. yr^{-1} averaged over all glaciers in Svalbard for the period 1957–2014 and standard deviation (σ_{time}) of the temporal variability, temporal correlation with B_{clim} ($R_{B_{clim}}$), trend slope (β) in cm w.e. yr^{-2} and slope uncertainty ($2\sigma_{slope}$). Slope significance at the 95 % level in bold font ($|\beta| > 2\sigma_{slope}$).

Variable	Mean	σ_{time}	$R_{B_{clim}}$	β	$2\sigma_{slope}$
B_{clim}	8.2	34.2	1.00	**−1.35**	0.41
Snowfall	61.3	9.3	0.32	0.10	0.14
Rime	1.1	0.3	−0.38	**0.01**	0.00
Refreezing	21.5	3.7	0.62	**−0.12**	0.05
Melt	−72.4	30.2	0.93	**−1.35**	0.32
Sublimation	−1.6	0.2	−0.20	**0.00**	0.00

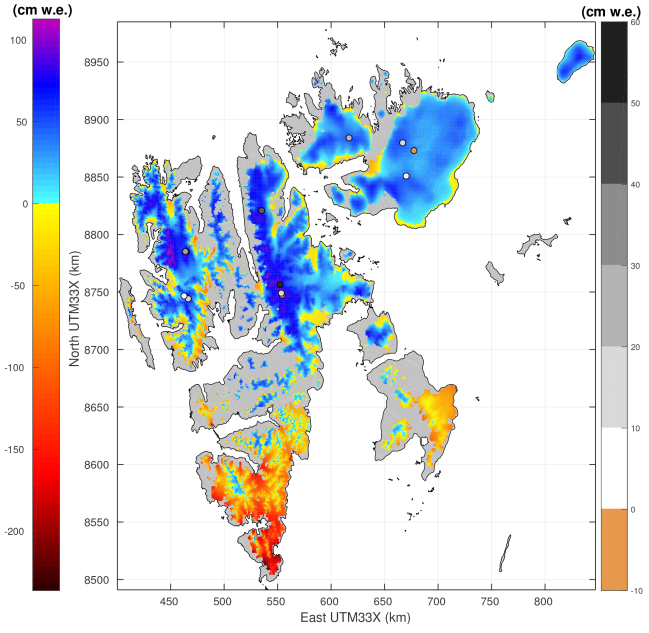

Figure 6. Map of simulated specific climatic mass balance (B_{clim}) averaged for the period 1957–2014 in cm w.e. yr^{-1} (colour scale on the left side). Circles indicate difference between modelled B_{clim} and the ice-core-derived B_{clim} (colour scale on the right side). For several ice cores, mass balance estimates are available for different time periods; here we only show the longest period; see Table 7 for details.

5 Results

5.1 Climatic mass balance

The modelled mean annual B_{clim} averaged over the entire domain for the period 1957 to 2014 is positive (8.2 cm w.e. yr^{-1}), which corresponds to a mass gain of 3.1 Gt yr^{-1} using the current glacier mask of each year. However, there is considerable temporal and spatial variability (Fig. 6). We find glacier-wide mass loss for many southern Spitsbergen glaciers. In contrast, northern Spitsbergen and Nordaustlandet have positive B_{clim}, and in some cases the ELA reaches sea level. The components of the climatic mass budget averaged over all glaciers and the 1957–2014 period are shown in Table 4. Ablation is dominated by melt (98 %), while refreezing is a major component (26 %) of the total accumulation.

The temporal variations of the glacier-wide annual balances and their components are shown in Fig. 7. Despite overall positive B_{clim}, there is a clear negative trend of -14 ± 4.1 cm w.e. $decade^{-1}$ over the entire period 1957–2014. Since we identified some weakness in the ERA40 data (see Sect. 6.3) we extract the B_{clim} trend for the ERA-Interim period 1979–2014, which yields a trend of -9.6 ± 9.9 cm w.e. $decade^{-1}$ that is not significant at the 95 % level. Melt is well correlated ($R^2 = 0.93$) with B_{clim}, and controls both B_{clim} interannual variability and the trend. Accumulation has a small increase (not significant at 95 % level) over the period, while there is a significant decrease in refreezing.

5.2 Surface energy balance variability with climate

Figure 8 shows mean melt season (15 May to 30 September) energy fluxes for each year from 1958 to 2014. Shortwave and longwave radiation balances are relatively small compared to glaciers at lower latitudes, 28 and -21 W m^{-2} respectively. Due to the late melt season onset over a larger part of Svalbard, little melt occurs in May and in the first half of June. This results in a negative radiation balance, even on sunny days due to high albedo and longwave radiative cooling. S_{net} and Q_H are the main energy sources for melt, although all fluxes but Q_G contribute during strong melt events, such as during summer cyclones. Over the model period, there is a decrease in solar insolation ($S_\downarrow$) and an increase in $L_\downarrow$, indicating cloud thickening (Table 5). Despite reduced insolation, S_{net} increases over the time period due to a decrease in albedo. Because of increased summer temperatures, Q_H increases over the period, with a maximum during the warm 2013 melt season. Average Q_L is close to zero in the 1960s, while it has been mostly positive since 1970. Both the turbulent fluxes have a significant increase over the period. Q_G decreases over the period, which we associate with the reduction of snow and firn volumes. Glacier ice has a higher thermal conductivity than snow and firn, such that heat exchange is more efficient between the surface and the subsurface layers. In addition, higher conductivity during winter enables efficient cooling of the near-surface layers. The energy flux for melt increases over the study period by 3.8 ± 1 W m^{-2} per decade. This trend is significant despite large year-to-year variability. During the 1960s, mean Q_M (-13 W m^{-2}) was less than half of that after 2000 (-30 W m^{-2}).

Annual sums (Σ) of positive degree days (PDD) increase from 82 K d during the 1960s to 213 K d as the 2000–2014 average. Over the same period, the increase in melt is of similar magnitude, rising from 48 to 110 cm w.e. yr^{-1}. There is

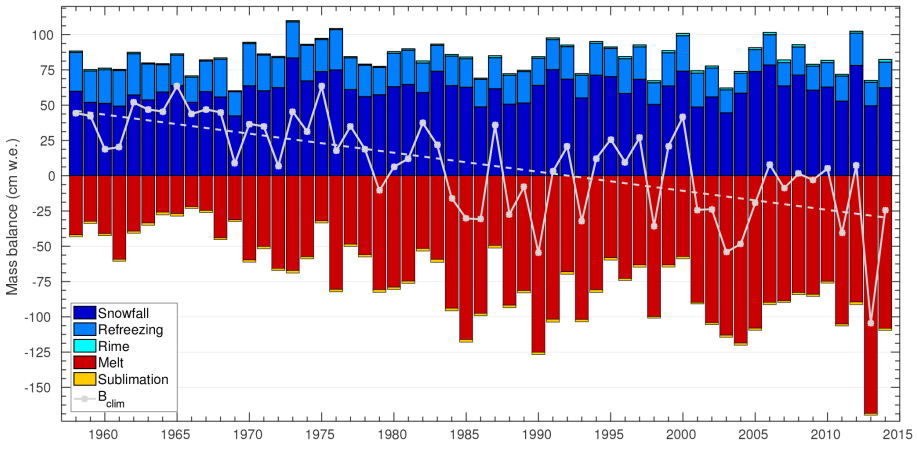

Figure 7. Annual specific climatic mass balance (B_{clim}) and its components, 1957–2014. Area averaging is performed using the temporal glacier mask. Dashed line is the linear mass balance trend of -14 ± 4.1 cm w.e. yr^{-1} decade^{-1}, with uncertainty referring to 2 standard deviations.

Table 5. Summary of modelled energy fluxes (W m^{-2}) averaged over all glaciers and each year's melt season (15 May–30 September) for the period 1957–2014. SD is 1 standard deviation of the temporal variability, $R_{Q_{\mathrm{M}}}$ is the correlation with Q_{M} over the melt season, β is the estimate of a linear trend over 1957–2014, and σ_{slope} is slope uncertainty given by 2 standard deviations. Slopes significant at the 95 % level are marked in bold ($|\beta| > 2\sigma_{\mathrm{slope}}$).

Variable	Mean (W m^{-2})	SD (W m^{-2})	$R_{Q_{\mathrm{M}}}$ (–)	β (W m^{-2} yr^{-1})	$2\sigma_{\mathrm{slope}}$ (W m^{-2} yr^{-1})
$S_{\downarrow}$	161	9.4	0.21	−0.07	0.15
$S_{\uparrow}$	−133	9.2	−0.62	**0.24**	0.13
$L_{\downarrow}$	281	5.8	−0.56	0.08	0.09
$L_{\uparrow}$	−303	3.0	0.60	**−0.06**	0.05
Q_{H}	12.2	3.1	−0.87	**0.13**	0.04
Q_{L}	1.2	1.7	−0.93	**0.07**	0.02
Q_{G}	−3.9	1.0	0.41	**−0.03**	0.01
Q_{R}	0.1	0.1	−0.80	0.00	0.00
α (%)	82.7	2.6	0.97	**−0.11**	0.03
Q_{M}	−22.6	8.9	1.00	**−0.38**	0.10

a very weak correlation ($R = 0.13$) between winter snow accumulation and B_{clim}. A much higher correlation of 0.55 is found between summer snowfall and B_{clim}, which is linked to its effect on both albedo and refreezing. The correlation between PDD and snow accumulation is smaller (−0.40) such that the low temperatures alone cannot explain the summer snowfall effect. Of all the glacio-meteorological variables in Tables 5 and 6, PDD and albedo are the quantities that can explain B_{clim} best. Q_{L} is relatively small, but it is surprisingly well correlated to both melt and B_{clim}. In the Q_{L} calculation, humidity and temperatures in the air and at the surface are included together with wind speed, thereby integrating several relevant meteorological variables.

5.3 Refreezing and subsurface properties

Overall refreezing comprises 26 % of total accumulation, but the amount of refreezing is reduced by 1.2 cm yr^{-1} decade^{-1} over the period. With the slight increase of snowfall, the role of refreezing is reduced from 29 % of the accumulation in the 1960s to 22 % in the 2000s. The refreezing also has a profound effect on the subsurface thermal regime. When meltwater percolates and refreezes, it releases large amounts of latent heat; at the same time, densification leads to an increase in thermal conductivity, thereby intensifying heat conduction.

Through refreezing and prolonged negative B_{clim}, subsurface density and temperature change markedly over the period. Figure 9 shows that refreezing increases with altitude, with large interannual variability. During the cold 1960s there is decreasing refreezing with altitude above 500 m elevation. In this case, refreezing is limited by available water; Fig. 9b indicates the presence of cold firn for these areas. After 1975, Svalbard accumulation areas are mostly temperate or near temperate at 15 m depth. Transition from cold to

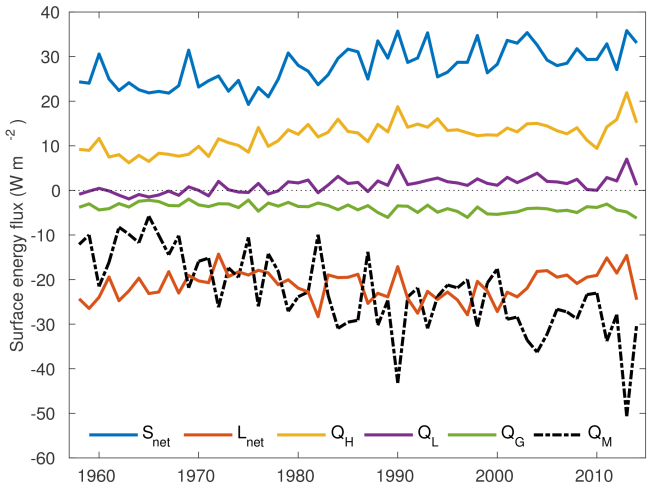

Figure 8. Modelled energy fluxes ($\mathrm{W\,m^{-2}}$) averaged over all glaciers and each year's melt season (15 May–30 September) for the period 1957–2014. Area averaging was performed based on each year's glacier mask.

Table 6. Glacio-meteorological variables averaged over all glaciers in Svalbard and the period 1957–2014 separated into: annual, melt season (15 May–30 September) and accumulation season (1 October to 14 May) which are indicated by subscripts: A, S and W respectively. σ_{time} is 1 standard deviation of the temporal variability, $R_{B_{\mathrm{clim}}}$ is correlation with annual B_{clim}, β is the estimate of a linear trend, while σ_{slope} is slope uncertainty given by 2 standard deviations. Slope significance at the 95 % level in bold font ($|\beta| > 2\sigma_{\mathrm{slope}}$). Snow and rain is seasonal solid and liquid precipitation respectively. T is air temperature 2 m above the surface, $\sum$PDD is cumulative positive degree days calculated from T_{A} and α is the melt season albedo.

Variable	Unit	Mean	σ_{time}	$R_{B_{\mathrm{clim}}}$	β	$2\sigma_{\mathrm{slope}}$
$\mathrm{Snow_W}$	mm w.e.	468	78.1	0.13	**1.70**	1.16
$\mathrm{Snow_S}$	mm w.e.	146	35.0	0.55	**−0.65**	0.53
$\mathrm{Rain_W}$	mm w.e.	23.2	14.9	0.01	0.05	0.24
T_{A}	°C	−9.00	1.5	−0.49	**0.07**	0.02
T_{S}	°C	0.23	0.8	−0.85	**0.03**	0.01
T_{W}	°C	−12.1	1.9	−0.41	**0.08**	0.02
$\sum$PDD	d °C	152	59.6	−0.89	**2.77**	0.60
α	%	82.7	2.6	0.96	**−0.11**	0.03

temperate firn is accompanied by a seasonal shift of the main refreezing period. In cold firn, most of the refreezing occurs when percolating water enters cold subsurface layers. While in the temperate firn, a large portion of the refreezing occurs when capillary water refreezes as the firn cools during winter. As the ELA increases, firn area extent is reduced and, accordingly, the potential for heat release through refreezing is also reduced. Henceforth, glacier areas that lose firn due to raised ELA experience subsurface cooling. This occurs at different altitudes around Svalbard, consistent with the regional ELA pattern. In north-eastern Svalbard cooling occurs above

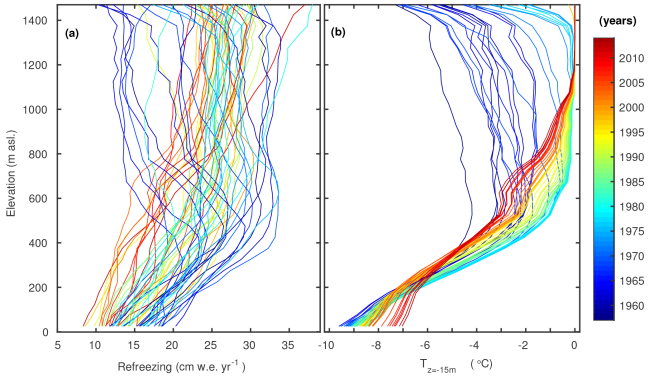

Figure 9. (a) Refreezing rate and **(b)** mean annual temperatures at 15 m depth averaged over 50 m altitude intervals from 1957 (blue) to 2014 (red).

100 m a.s.l., while cooling starts at 450 m a.s.l. in southern Spitsbergen. Figure 9 shows the expansion of the cold ice area, which is predicted for polythermal glaciers in a warming climate, and also shown in model experiments (Irvine-Fynn et al., 2011; Wilson and Flowers, 2013). The regionally differentiated thermal response is shown in Figs. S6 and S7.

In contrast to the firn area, refreezing in the ablation area results in the formation of superimposed ice. Below the ELA, the newly formed superimposed ice ablates later during the same melt season. Figure 10 shows annual area-averaged refreezing, superimposed ice (SI) and internal accumulation, which refers to refreezing below the previous summer surface. Over the period there is a decrease in internal accumulation following the firn area decrease. The reduction in internal accumulation is only partly compensated for by refreezing above the previous summer surface. Thus, total refreezing decreases over the period, whereas the amount of SI formation in the SI zone is quite stable, except in very negative years, when nearly all formed SI ablates later in the melt season.

The area covered by thick firn (dark blue, Fig. 10b) decreases over the period, except for small increases in the late 1960s and around 2000. Annual variability of glacier facies is almost exclusively due to the variability of the thin firn and superimposed ice zone, with the thin firn area increasing during years of positive B_{clim} and vice versa. Similar fluctuations are seen for the firn bulk density, in which the firn is densifying during years of negative B_{clim}. Hence, the respective densities of the thin and thick firn reveal similar evolution to those of the firn area extent, with year-to-year fluctuations for the thin firn and dampened decadal variations for the thick firn.

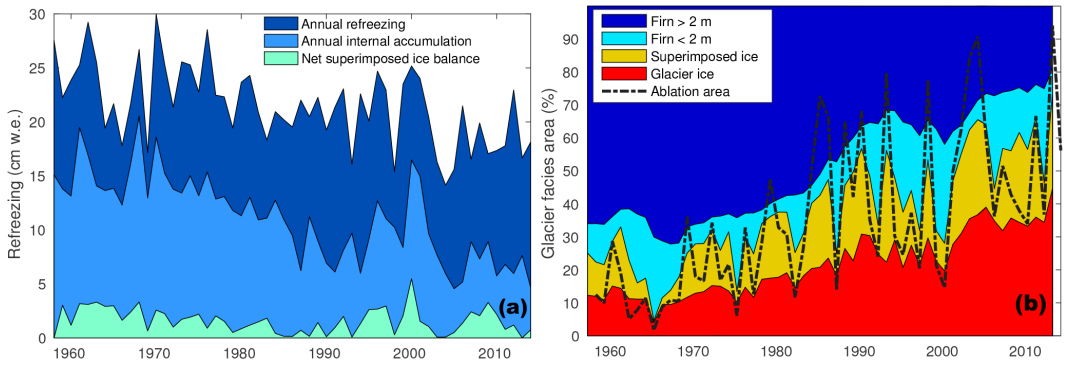

Figure 10. (a) Annual refreezing and internal accumulation (i.e. refreezing below the previous summer surface) and the net superimposed ice balance, i.e. the amount of superimposed ice at the end of each mass balance year. **(b)** Annual fractional areal extent of glacier facies divided into glacier ice, superimposed ice, thin firn (< 2 m) and thick firn (> 2 m).

Table 7. Climatic mass balances derived from ice cores (B_{clim}) (cm w.e. yr^{-1}) from Pinglot et al. (1999, 2001) and error ϵ (modeled − measured) for the three time periods. Z is elevation of the ice core and Z_ϵ is elevation of the closest DEM grid cell minus ice core elevation. The year of ice core retrieval depends on the site and is denoted by 199X; see Pinglot et al. (1999, 2001) for exact years. The error is positive if modelled balance is larger than measured.

					1963–1986		1986–199X		1963–199X	
Location	Longitude °E	Latitude °N	Z m a.s.l.	Z_ϵ m	B_{clim} cm w.e. yr^{-1}	ϵ	B_{clim} cm w.e. yr^{-1}	ϵ	B_{clim} cm w.e. yr^{-1}	ϵ
Kongsvegen-K	13.3	78.8	639	−39	50	6	48	−8	48	7
Kongsvegen-L	13.4	78.8	726	17	59	14	62	−11	60	10
Snofjella-M	13.3	79.1	1170	−24	–	–	57	14	–	–
Snofjella-W	13.3	79.1	1190	−44	37	52	–	–	47	39
Vestfonna	21.0	80.0	600	2	46	17	41	0	38	20
Aust-98	24.0	79.8	740	12	48	−4	52	−24	50	−10
Lomonosov-76	17.5	78.8	1000	32	–	–	–	–	82	30
Lomonosov-s8	17.5	78.8	1173	−54	–	–	75	16	–	–
Lomonosov-s10	17.4	78.9	1230	12	–	–	–	–	36	59
Aasgaardsfonna	16.7	79.5	1140	−98	–	–	–	–	31	40
Aust-F	23.5	79.9	727	−4	–	–	37	10	–	–
Aust-D	23.5	79.6	708	−54	–	–	34	1	–	–
Average					48	17	48	1	49	24

5.4 Model validation and sensitivities

Mass balance from stakes and ice cores

The overall model performance in terms of B_{clim} is determined by comparing stake mass balance readings and mass balance retrieved from ice cores with the model grid box closest to the measuring site. In total, there are 1459 annual mass balances measurements covering different time periods at the various locations; see Sect. 2 and Table 7 for specifications. For all these measurements, the model slightly underestimates B_{clim} by 1 cm w.e. yr^{-1}. However the much higher RMSE of 59 cm w.e. yr^{-1} reveals the existence of compensating errors. At Hansbreen, mass balance is underestimated by more than 100 cm w.e. yr^{-1} in some years, while mass balance is overestimated at the lower stakes of the other three Spitsbergen glaciers. This is illustrated in Fig. 11, which also shows that modelled mass balance gradients are too low for all five glaciers.

Mass balance measurements used in the calibration for the period 2004–2013 at Kongsvegen, Etonbreen and Hansbreen correspond to about 25 % of the total measurements. When removing the measurements used for calibration, the RMSE is slightly reduced (58 cm w.e. yr^{-1}). Since we apply equal weights to all measurements the impact of Hansbreen (the region with large underestimation) is reduced, thereby improving the RMSE.

The model generally overestimates B_{clim} (Table 7) at the ice core sites, in contrast to the stakes. At the higher elevations of Holtedahlfonna, Nordenskiöldbreen, and Kongsvegen, Fig. 11 shows that B_{clim} and winter balance are under-

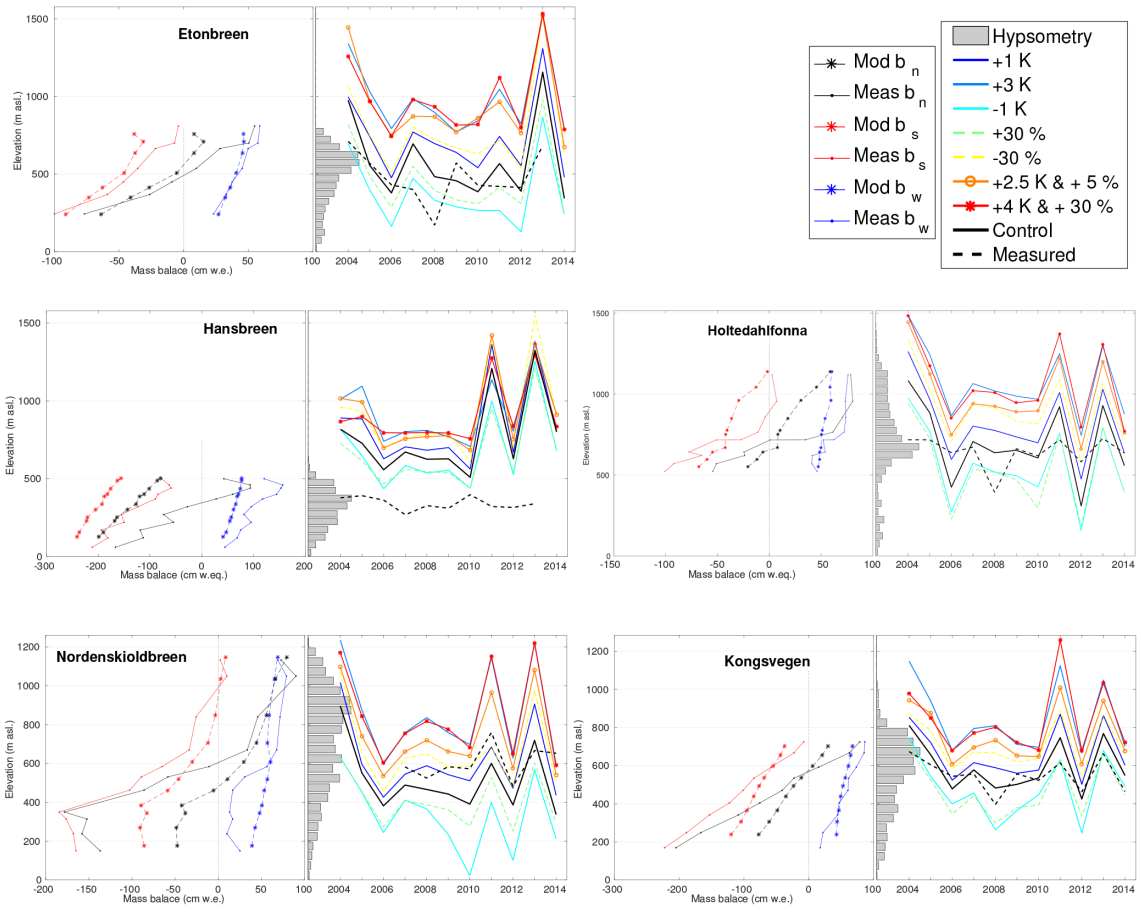

Figure 11. Modelled and measured seasonal mass balance gradients (left panels of each glacier's subplot) at the five validation glaciers averaged over the period 2004–2013 (right panels). Modelled results include the control run and sensitivity experiments. Dots and stars mark the altitudes of the measurement sites and corresponding DEM grid cells respectively. Grey bars show area-altitude distribution for 50 m elevation bins. Note that the mass balance measurements at Kongsvegen, Etonbreen and Hansbreen over 2004–2013 also are used for model calibration.

estimated. Although mass balance stakes at these glaciers are in the proximity of the drilling sites, there is no overlap in period, since the ice cores were retrieved at about the same time that the adjacent mass balance programmes began. Assuming that both stake and ice core-derived mass balance measurements are correct, model error is not time invariant at these sites. Ice-core-derived mass balances at Holtedahlfonna increased over the period 1963–1991, while no change is found at Kongsvegen for this period (Table 7). Over the same period, modelled B_{clim} decreases slightly due to higher melt rates.

To test the possible presence of a trend in the model performance, we compared the mass balance measured by a stake at 380 m elevation on Midtre Lovenbreen, a small glacier south-east of Ny-Ålesund, to the modelled B_{clim} of a nearby pixel with the corresponding altitude. There is a good correlation between the two records, although the model overestimates B_{clim} throughout the record from 1968–2014. However, after 2000 there is hardly any bias, while B_{clim} is overestimated by about 40 cm w.e. yr^{-1} for the period 1968–1979. This trend in model performance is driven by melt, and therefore most likely by summer air temperatures. Although B_{clim} is overestimated, winter accumulation is underestimated in the model, which can be attributed to overestimation of sea ice in the reanalysis product on the northwestern coast of Spitsbergen. The west coast is usually ice-free year round, but prior to 1979 satellite data were not available to constrain sea ice cover and sea surface temperature in the reanalysis. An erroneous sea ice cover influence the heat and moisture uptake in the reanalyses, from which our forcing data were derived.

5.5 Sensitivity experiments

5.5.1 Model parameters

Due to large computational cost, sensitivity experiments are limited to stake locations on the five target glaciers over the period 2004–2013. In contrast to the calibration procedure,

Table 8. Sensitivity of the climatic mass balance B_{clim} in response to perturbations of model parameters and climate perturbations. dB_{clim} (cm w.e.) is the departure of B_{clim} from the control run averaged over all stakes and years, σ (cm w.e.) is the standard deviation of the difference for both year to year and site to site. α is albedo, t is ageing factor for snow albedo, $T_{rain/snow}$ is rain snow threshold, z_0 is roughness lengths for momentum necessary for calculating the turbulent heat fluxes. Climate experiments are given by uniform air temperature shifts (K) and precipitation increases (%), but for the last two experiments we apply seasonal differences; see text for explanation.

Parameter	Control	Perturbation	Response	
			dB_{clim}	SD
α_{ice}	0.3	+0.05	0.4	6.1
		−0.05	−0.7	6.9
α_{snow}	0.85	+0.05	5.6	6.7
		−0.05	−6.4	7.5
α_{firn}	0.62	+0.05	7.1	7.2
		−0.05	−7.1	7.5
t^*	{5, 15, 100 d}[a]	× 0.5	−8.3	7.7
		× 2	9.4	7.3
z_0	{0.18, 0.06 mm}[b]	× 0.5	6.5	8.2
		× 0.25	12.7	11.2
		× 2	−7.1	7.8
		× 4	−14.0	11.3
$T_{rain/snow}$	1.5	−1 K	−3.8	8.1
		+1 K	7.9	9.3
Temperature		+1 K	−29.7	20.8
		+2 K	−64.7	38.7
		+3 K	−109.0	61.3
		−1 K	29.9	18.7
		−2 K	61.3	35.0
		−3 K	87.7	52.1
Precipitation		+15 %	13.1	8.0
		+30 %	25.2	9.4
		−15 %	−14.2	7.6
		−30 %	−29.7	10.4
Førland (2011)[c]		+4 K and +5 %	−81.7	49.4
Førland (2011)[d]		+6 K and +30 %	−134.4	87.4

[a] Timescales of ageing are 5, 15 and 100 days at temperatures of 0 °C (wet), 0 °C (dry) and −10 °C. [b] Roughness lengths for ice and snow respectively. [c, d] Climate scenario for western and north-eastern Svalbard respectively, as in Førland et al. (2011).

here we perturb one parameter at a time to isolate its effect. Table 8 show parameters used in the control run, the perturbation and the B_{clim} response averaged over all stakes and years, relative to the control run (dB_{clim}) and the geographical variability at all mass balance stake locations in terms of standard deviation (SD). The sensitivity of ice albedo is surprisingly low in comparison to other parameters, while albedo-ageing parameters (t^*) have rather large impact on B_{clim}. This can be explained by the relatively short exposure of glacier ice at the surface. Even in the ablation area, snowfall is common during the melt season, such that the rate of albedo decay is more important than the actual threshold values. The modelled B_{clim} is robust with respect to the choice of roughness lengths (z_0). A 1 K change in the rain–snow threshold temperature has a comparable effect as a 10 % precipitation change. More than 90 % of this change takes place during the melt season. Although a large portion of the precipitation occurs at temperatures close to the phase transition, the effect of the rain–snow threshold on winter mass balance is not so important in terms of mass balance, since most of the winter rain refreezes.

5.5.2 Climate

We explore the sensitivity of the climatic balance to climate change by applying uniform perturbations in temperature and precipitation to the climate data for the period 2004–2013. First we shift air temperature by ±1, ±2 and ±3 K and then increase precipitation by ±15 and ±30 %, leaving temperature unperturbed. A temperature increase of 1 K results in a B_{clim} decrease of 30 cm w.e., which is the same as found by van Pelt et al. (2012). The temperature sensitivity of roughly $-30\,\mathrm{cm\,w.e.\,yr^{-1}\,K^{-1}}$ is in the lower range reported from glaciers elsewhere in the world (see De Woul and Hock, 2005 and references therein). However, the impact of this low sensitivity on B_{clim} is higher than for other glacierized regions given the low mass flux turnover in Svalbard. This is exemplified by comparing the impact of a temperature perturbation on the mass balance components of the control run over the 2004–2013 period, wherein a temperature increase of 1 K results in a 30 % increase in ablation and more than doubled the already negative B_{clim}. A precipitation increase of nearly 40 % would be necessary to compensate for a temperature increase of 1 K.

We also perform two perturbations which correspond to temperature and precipitation projections for 2100 after Førland et al. (2011). Since changes in temperature and precipitation at Svalbard are projected to occur with a substantial south-west to north-east gradient, we perform two experiments. In the first scenario, we increase annual temperature and precipitation by 4 K and 5 % respectively, to represent changes as expected for western Svalbard. In the second scenario, applicable for north-eastern Svalbard, we use annual increases of 6 K and 30 % precipitation. For these future scenarios we apply seasonality in air temperature, as suggested in Førland et al. (2011), with summer temperature increase of 2.5 K for western Svalbard and 4 K for north-eastern Svalbard. Figure 11 shows that the modelled ELA on the measured glaciers is mostly above the present topography under both scenarios. Note that the predictions of Førland et al. (2011) are for 2071–2100 averages relative to the normal period 1961–1990. We apply these increases to the 2004–2013 period, which has an annual air temperature of −3.2 °C, already 3.5 K warmer than the normal period (1961–1990).

5.5.3 Glacier mask

We test the impact of choice of glacier mask on B_{clim} by applying the three different fractional glacier masks (Sect. S2); the reference mask (all-time max), the 2000s mask and the time-varying mask. B_{clim} for the whole of Svalbard is 4.5 cm w.e. yr^{-1} for the reference mask, 10 cm w.e. yr^{-1} for the 2000s mask and 8.2 cm w.e. yr^{-1} for the time-varying mask. Despite relatively small differences in area and specific mass balance, there is a 100 Gt ice mass difference over the 56-year period for the different glacier masks. In comparison this is more than a third of the annual contribution of all glaciers and ice caps to sea level rise. Since the area difference between the glacier mask mainly occurs in the lower ablation zone, where B_{clim} fluxes are the largest, a small area change has a substantial impact on the glacier-wide B_{clim}. Hence, accurate representation of glacier margins in B_{clim} models are very important. Mass balance using the time-varying mask represents something between the conventional and reference surface mass balance (Elsberg et al., 2001), since glacier area is annually updated, while the DEM is static.

6 Discussion

6.1 Controls on B_{clim} at present and in a warmer climate

Variability in annual B_{clim} is found to be dominated by summer melt, thereby confirming other studies at Svalbard (Lang et al., 2015a; van Pelt et al., 2012). Melt variability is driven by melt season air temperatures. Albedo, which shows the largest correlation with B_{clim} (Tables 4 and 9), is closely related to net shortwave radiation, the largest energy source for melt. Albedo is also indicative of winter snow and summer snowfall events, since it has higher values for snow than for bare ice (Table 9), but is also related to temperature through the precipitation phase, rate of albedo decay and the importance of temperature for melt.

With a future climate as projected by Førland et al. (2011), increased precipitation can only partly compensate for enhanced melting. Lang et al. (2015b) argue that increases in future cloud cover will reduce the negative effect of a warming climate on B_{clim}. Statistics of our simulations show that the net radiation is positively correlated with summer air temperatures (Table 9), suggesting that increased cloud cover lead to higher net radiation through longwave radiation despite a decrease in shortwave radiation. Cloud cover is not specifically addressed in our sensitivity test and an extrapolation to the future is hence afflicted with large uncertainties.

As in Greenland, melt water retention through refreezing in Svalbard has been proposed as an efficient buffer for mass losses in a future warmer climate (Harper et al., 2012; Wright et al., 2005). However, here we find that refreezing and re-

Table 9. Correlation coefficients between annual mass balance components, average melt season surface energy fluxes and selected meteorological variables. B_{ACCU} and B_{ABLA} are total annual accumulation and ablation respectively and B_{ref} is annually refrozen water. Precipitation is separated into snow and rain where indices s refers to summer averages (15 May–31 September) and w refers to the period 1 October–14 May. T_A and T_S are annual and summer averages of near-surface air temperature over the entire glacier area respectively.

	B_{clim}	B_{ACCU}	B_{ABLA}	B_{ref}	Q_N	$S_\downarrow$	$L_\downarrow$	Q_H	Q_E	Q_G	α	$Snow_w$	$Snow_s$	$Rain_w$	T_A	T_S	ΣPDD
B_{clim}	1.00	0.48	0.95	0.62	−0.31	0.05	−0.46	−0.78	−0.86	0.35	0.96	0.13	0.55	0.01	−0.49	−0.85	−0.89
B_{ACCU}	–	1.00	0.19	0.53	−0.61	−0.39	−0.10	0.02	−0.15	−0.13	0.36	0.84	0.60	0.27	0.27	−0.20	−0.12
B_{ABLA}	–	–	1.00	0.51	−0.14	0.19	−0.48	−0.88	−0.91	0.43	0.95	−0.15	0.41	−0.09	−0.64	−0.88	−0.95
B_{ref}	–	–	–	1.00	−0.35	−0.06	−0.33	−0.37	−0.46	−0.05	0.59	0.10	0.37	0.30	−0.30	−0.53	−0.50
Q_N	–	–	–	-	1.00	0.79	−0.06	−0.01	0.13	0.02	−0.31	−0.38	−0.65	−0.09	−0.13	0.07	0.07
$S_\downarrow$	–	–	–	–	–	1.00	−0.66	−0.16	−0.17	−0.05	0.10	−0.36	−0.35	−0.13	−0.36	−0.37	−0.30
$L_\downarrow$	–	–	–	–	–	–	1.00	0.24	0.43	0.11	−0.54	0.12	−0.22	0.10	0.43	0.68	0.58
Q_H	–	–	–	–	–	–	–	1.00	0.92	−0.52	−0.79	0.27	−0.22	0.01	0.59	0.68	0.87
Q_E	–	–	–	–	–	–	–	–	1.00	−0.40	−0.87	0.17	−0.40	−0.01	0.54	0.76	0.89
Q_G	–	–	–	–	–	–	–	–	–	1.00	0.43	−0.24	0.27	0.03	−0.41	−0.35	−0.45
α	–	–	–	–	–	–	–	–	–	–	1.00	−0.04	0.59	−0.02	−0.58	−0.89	−0.94
$Snow_w$	–	–	–	–	–	–	–	–	–	–	–	1.00	0.20	0.25	0.59	0.15	0.23
$Snow_s$	–	–	–	–	–	–	–	–	–	–	–	–	1.00	−0.06	−0.25	−0.43	−0.41
$Rain_w$	–	–	–	–	–	–	–	–	–	–	–	–	–	1.00	0.44	0.07	0.15
T_A	–	–	–	–	–	–	–	–	–	–	–	–	–	–	1.00	0.63	0.73
T_S	–	–	–	–	–	–	–	–	–	–	–	–	–	–	–	1.00	0.91
ΣPDD	–	–	–	–	–	–	–	–	–	–	–	–	–	–	–	–	1.00

tention decrease over the 1957–2014 period, both in absolute numbers and as a percentage of the B_{clim}. These findings are in line with other studies in Svalbard (van Pelt and Kohler, 2015) and Greenland (Charalampidis et al., 2015; Machguth et al., 2016). Even if the superimposed ice area increases, at the expense of the firn area, superimposed ice formation does not compensate for the loss of internal accumulation. In contrast to the Greenland ice sheet, the existing area of cold firn in Svalbard is not large enough to buffer effects of future warming. Furthermore, our model does not simulate impermeable ice layers within the firn; such layers would further decrease the available storage volume by diverting run-off laterally (Mikkelsen et al., 2015).

Despite an overall decrease in refreezing, some low-altitude areas along the western coast show an increase due to winter rain events (e.g. Hansen et al., 2014). During and in the first days after rain events substantial amounts of superimposed ice form. However, for the rest of winter, densification of the snowpack reduces the insulating effect such that the initial latent heat release is largely compensated if not exceeded by intensified cooling.

For a warmer climate, our results suggest a cooling of glacier ice close to the (rising) ELA. At the glacier front, modelled temperatures at 15 m depth increased by 2–4 °C over 1957–2014. It is likely that glaciers that have their snouts frozen to the ground will approach the melting point in the near future, if warming continues. Frozen glacier fronts may act as a plug for the upstream glacier flow and provide a mechanism to slow the entire glacier (e.g. Dunse et al., 2015). Furthermore, a thermal switch at the glacier base allows for sliding and is proposed as a surge initiation mechanism (e.g. Murray et al., 2000). Historical records show that surge frequency at Svalbard is connected with periods of warming and negative B_{clim} (W. Farnsworth, personal communication, 2015). Increased ice flow leads to more crevassing, which again promote cryo-hydrological warming and basal lubrication, acting as a positive feedback in the system (Phillips et al., 2010; Dunse et al., 2015). Although these mechanism are not fully understood, theory suggests that increased run-off and changes in the thermal and hydrological regimes may trigger widespread changes in the velocity structure of large ice masses. To further study the coupling between surface and basal processes, melt rates and near-surface temperatures must be reliably quantified; this requirement emphasizes further potential use of the data set resulting from our study.

6.2 Comparison to other studies

We compare our results to Svalbard-wide mass balance estimates by other studies (see Table 10), although direct comparability is hampered by differences in areal coverage or time periods due to lack of definition of areas in the other studies. Also some studies (e.g. based on gravimetric or geodetic methods) include all mass changes, i.e. also those caused by frontal ablation (e.g. mass loss due to calving and submarine melt).

Figure 12 shows mass balance through time compared with studies summarized in IPCC (2013) along with three other recent B_{clim}-studies. Average mass balance for the respective studies are also listed in Table 10. Overall there is a good agreement with the other studies, but our B_{clim} estimates are more negative than the others for the latter part of the study period, whereas the opposite is true during the first part. Our estimate is expected to be higher than the geodetic and gravimetric estimates since they account for mass loss by frontal ablation, which is estimated to be 13 ± 5 cm w.e. yr^{-1} (Błaszczyk et al., 2009). Compared to Nuth et al. (2010), our estimate is 30 cm w.e. yr^{-1} less negative due to more positive B_{clim} in north-eastern Spitsbergen. In the same area, ice-core-derived B_{clim} also suggest that our model overestimates B_{clim}, indicating too-high precipitation and/or too-low air temperature in our forcing data set for this region. The north–south gradient in downscaled mean annual air temperatures is twice as large as that observed at weather stations in Hornsund, Longyearbyen and Ny-Ålesund. The exaggerated horizontal temperature gradient (Fig. 4b) is possibly linked to the incorrect position of the sea ice edge in the ERA reanalysis (Aas et al., 2016). During summer, observations show that the southernmost station (Hornsund) is coldest, since the other two have a more continental climate. Continental warming in broad ice-free valleys is not well captured by the downscaling, due to a mismatch of the sea–land–glacier mask between the coarse reanalysis grid and the finer downscaled grid. This results in too-low temperatures at glacier fronts in the interior of Spitsbergen and consequent underestimation of ablation rates.

6.3 Uncertainties

Uncertainties are introduced at every step in the process chain and accumulate in the simulated B_{clim}. Uncertainties comprise the climate forcing and initial state, model set-up and parameterizations, topographic simplification and uncertainties of the measurements used for calibration. However, it is hard to quantify the contribution of the individual sources, especially since the calibration may compensate for systematic errors.

Glaciological surface mass balance represents a useful quantity for validating our model. Not only because it resembles our goal, mass balance, but it is sensitive to atmospheric and surface conditions over a large variety of temporal and spatial scales, thus is highly valuable for validating land surface models in general. Since subsurface properties (temperature, density and water content) are usually not well captured by glaciological mass balance measurements, the measurement uncertainty is higher in the firn areas compared to the 10 cm w.e. yr^{-1} uncertainty for glacier ice areas (Sect. 4.4).

Table 10. Svalbard mass balance estimates from different studies and methods. Note that the numbers between the studies are not directly comparable due to difference in time periods, areal coverage and methodology. Mass balance method short names are as follows: ICESat, a laser altimetry from the Ice, Cloud and elevation Satellite; GRACE, a gravimetry using data from the Gravimetry Recovery and Climate Experiment; Mix, a combination of GRACE, ICESat and modelling; WRF, MAR and RCM, three different regional climate models; Local is direct glaciological measurements; see references for details. Gravimetry studies report total mass balance (B_{tot}), which is the sum of climatic (B_{clim}), basal balance (B_b) and frontal ablation (A_f), The geodetic studies report (B_{tot}) by integrating elevation changes over a constant area ($B_{tot(A=const)}$). Other studies report climatic mass balance (B_{clim}) or surface mass balance (B_{sfc}). Except for our study, the B_{clim} and B_{sfc} studies assume constant glacier area, though the glacier area may vary between studies.

Period	This study cm w.e. yr^{-1}	Other studies cm w.e. yr^{-1}	B	Method	Reference
2003–2008	−13.4	-12 ± 4	$B_{tot(A=const)}$	ICESat	Moholdt et al. (2010)
2003–2010	−9.3	-9 ± 6	B_{tot}	GRACE	Jacob et al. (2012)
2003–2008	−20.2	-34 ± 19	B_{tot}	GRACE	Mèmin et al. (2011)
2003–2009	−11.6	-13 ± 6	B_{tot}/B_{clim}	Mix	Gardner et al. (2013)
2003–2013	−20.6	−25.7	B_{clim}	WRF	Aas et al. (2016)
2000–2011	−18.8	-5 ± 40	B_{clim}	RCM	Möller et al. (2016)
1979–2013	−7.8	−5.4	B_{clim}	MAR	Lang et al. (2015a)
1965/71/90–2005*	−5.8	-36 ± 20	$B_{tot(A=const)}$	Geodetic	Nuth et al. (2010)
1970–2000	8.5	-1.4 ± 0.3	B_{sfc}	Local	Hagen et al. (2003b)
1970–2000	8.5	-27 ± 33	B_{sfc}	Local	Hagen et al. (2003a)

* Start of time series depends on location; see Nuth et al. (2010) for details.

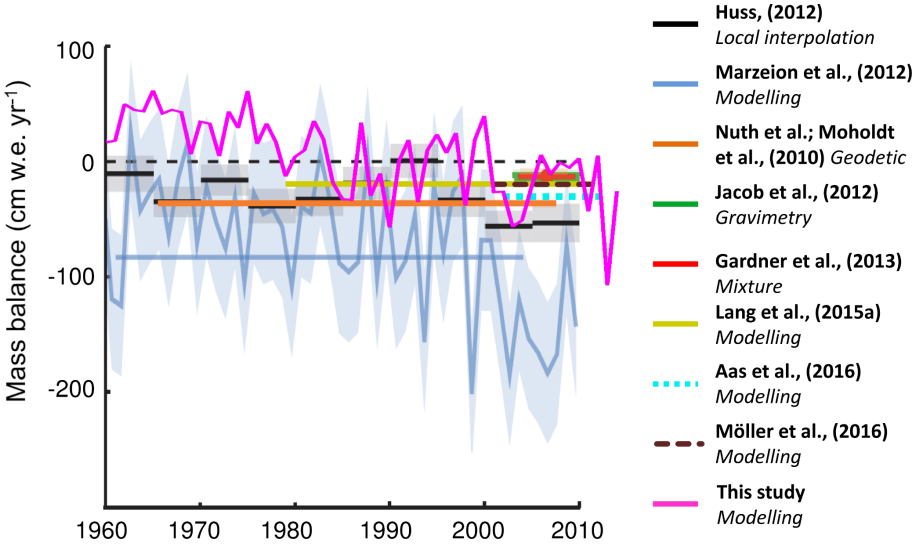

Figure 12. Svalbard mass balance estimates from different studies (bold font in legend) and methods (italic font). Shaded area of Huss (2012) and Marzeion et al. (2012) indicate the uncertainty. Figure modified from Vaughan et al. (Fig. 4.11. 2013)

Model performance at the validation sites (ice cores and stakes) is satisfactory with a mean bias of −1 cm w.e. yr^{-1}, but substantial compensating errors exist, as indicated by the RMSE of 59 cm w.e. yr^{-1}. For Svalbard as a whole, B_{clim} is in agreement with other studies, but regionally our B_{clim} is more positive in northern Spitsbergen and more negative in southern Spitsbergen.

Uncertainties in the climate forcing are probably the main source of error. We substantiate this statement with the impact of air temperature on B_{clim} (−30 cm w.e. yr^{-1} K^{-1}), the low sensitivity of model parameters (Sect. 5.5), and the ability of the model to reproduce measured B_{clim} when forced with local climate data at the weather station site (Østby et al., 2013). Validation at weather stations indicates that our climate forcing is of similar or slightly lower quality to other, more expensive downscaling studies (Claremar et al., 2012; Lang et al., 2015a; Aas et al., 2016).

Downscaled summer air temperatures are in general too low at the coastal weather stations (Table 2). In contrast, downscaled air temperatures are too warm at the glacier

weather stations. Theses biases, combined with the underestimation of summer mass balance gradients (Fig. 11), indicate too-low air temperature lapse rates in the downscaling. Since satellite-derived surface temperatures are capped at the melting point, only temperature measurements at elevation substantially higher than the ERA-orography can resolve this issue. The underestimated summer mass balance gradient may, at least partly, be explained by underestimated winter mass balance gradients (Fig. 11), through its effect of prolonged snow cover and increased albedo and refreezing.

Downscaled precipitation compares well to measurements at the coastal stations (Sect. 3.2.1) and seasonal precipitation is mostly well reproduced over the glaciers when compared to ice cores and winter mass balance from stakes and ground-penetrating radar. Underestimation of winter mass balance gradients (Fig. 11) is not necessarily indicative of too-low orographic enhancement in the LT model, but could be caused by wind redistribution. Snowdrift accumulates in concave-shaped accumulation areas, while the wind erodes ablation areas that tend to have a convex-shaped surface topography. In contrast, ice cores indicate that precipitation is overestimated at higher elevation in northern Spitsbergen. This bias could be caused by the wind-exposed ice core drilling sites at ice field summits. The largest precipitation underestimation (up to $100\,\mathrm{cm\,w.e.\,yr^{-1}}$) is found at Hansbreen, which is known to have an asymmetrical snow accumulation pattern across the centerline due to wind redistribution (Grabiec et al., 2006).

The TopoSCALE methodology for downscaling climate variables shows several shortcomings when applied to Svalbard. In the European Alps, where the methodology was developed, differences between the coarse reanalysis data and the finer grid for downscaling are governed by the elevation difference between the coarse and fine grid. in Svalbard, large horizontal gradients of atmospheric heat and moisture arise from the interaction between open water, sea ice, tundra and glacier-covered areas, in addition to the vertical gradients. Due to the coarse spatial resolution of the reanalysis, some land areas of our finer topography may be wrongly represented as ocean in the reanalysis, thereby considerably affecting the downscaled variables. For instance, land areas of southern Spitsbergen are largely represented as ocean in the ERA land mask, such that sea surface temperatures are incorporated into the downscaling of air temperatures over land and glaciers in the fine-scale topography. This gives rise to considerable biases and thereby also affects temperature gradients in the downscaled temperature field. A similar effect arises if an erroneous sea ice mask was employed in the reanalysis. The climate reanalysis is a quite homogeneous product in time, except for sea surface temperatures and sea ice cover, which have been substantially improved with the advent of satellite-borne sensors, and further improved with newer sensors. We link these improvements over time with the higher climate forcing quality after 1980 (Sect. 3.2.1). Nevertheless, this discontinuity in reanalysis quality coincides with the discontinuity of our composite forcing data set, which is based on ERA-40 before and ERA-Interim after 1979. To investigate the possibility that the resulting change in mass balance regime may be an artefact caused by this transition, simulations have been conducted over the overlap period 1979–2002 using both reanalyses, but only for the grid points used for calibration (Fig. 1). We find that the ERA40-based simulation yields an about 13 cm w.e. higher mass balance than the ERA-Interim-based one, but ERA-40-based simulations still show a 20 cm drop of B_{clim} between 1970 and 1990, larger than that caused by the data set discontinuity. This suggests that this change in mass balance regime is not caused by the heterogeneity of our composite forcing. Nevertheless, we cannot rule out the possibility that this change was caused by the discontinuity inherent in both reanalyses due to the availability of satellite observations after 1979 (Bromwich and Fogt, 2004; Screen and Simmonds, 2011; Uppala et al., 2005).

Calculations of turbulent fluxes and albedo are the processes within the model that have the highest sensitivities regarding parameter uncertainty on modelled B_{clim}. Model performance is quite robust to the choice of roughness lengths used to calculate turbulent fluxes, but values typically span several orders of magnitude in the literature. Albedo parameterization is shown to be more sensitive to the ageing parameters rather than the actual threshold values used in the parameterization. The applied albedo parameterization does not account for spatial variability due to impurity content, which is possibly a major weakness given that ice albedo varies from 0.15 to 0.44 across Svalbard (Greuell et al., 2007). Dark bands such as in western Greenland (Wientjes et al., 2011) are also observed in Svalbard, but are not included in the model. Extending the model albedo formulation to account for dust and impurity content would be a subject for future work. Model parameters concerning run-off and water retention may also be a significant error source, but we lack observational data to evaluate this aspect. The bucket-type water percolation method is also questionable, as infiltration is highly heterogeneous and horizontal fluxes are neglected (e.g. Reijmer et al., 2012; Cox et al., 2015). A 10-year spin-up time is found to be sufficient for the model performance, although sites close to the ELA showed a larger sensitivy to the spin-up period in the first years of the run (< 5 cm w.e.). From the Svalbard temperature record, we know that the 1960s were colder than the 1950s. Using the cold 1960s as a spin-up period has likely led to a too-large potential for refreezing given the lower temperatures of the early period. Additionally, lower temperatures cause less dense firn and further exaggerate the retention potential.

Although the 1 km-resolution DEM applied in this study largely reproduces the hypsometry of the 90 m DEM, glacier mask sensitivity reveals differences of $1.8\,\mathrm{Gt\,yr^{-1}}$ between different glacier masks (Sect. 5.5.3), slightly lower than the $2.1\,\mathrm{Gt\,yr^{-1}}$ mass loss from tidewater margin retreat (Błaszczyk et al., 2009). We assess possible errors introduced

by a static DEM by considering a typical mass balance gradient of 0.2–0.3 cm w.e. m^{-1}. A uniform elevation change of 10 m for the entire glacier surface would alter the mass balance by 2 cm w.e. yr^{-1}, equivalent to 1 Gt yr^{-1}. Observed elevation changes in southern and western Spitsbergen for 1930s to 1990s are typically a few tens of metres (Nuth et al., 2010). In the early part of the study period, when the DEM difference is largest, this error might amount up to 1 Gt yr^{-1}.

7 Conclusions

This study presents modelled climatic mass balance for all glaciers in Svalbard for the period 1957–2014. Modelled mass balance is mostly in line with previous studies. Despite overall good model performance, validation with in situ mass balance measurements indicate regionally compensating errors. Our main findings are as follows:

- Svalbard B_{clim} is estimated at 8.2 cm w.e. yr^{-1}, corresponding to a mass surplus of 175 Gt over the 1957–2014 period. Mass loss increases over the period and B_{clim} switches from a positive to negative regime around 1980, with a trend of -1.4 ± 0.4 cm w.e. yr^{-2}. For the ERA-Interim period 1979–2014, we find a trend in modelled B_{clim} of 0.96 ± 0.99 cm w.e. yr^{-2}, but it is not significant at the 95 % level. Current B_{clim} for the period 2004–2013, combined with frontal ablation estimates (Błaszczyk et al., 2009), yields a total Svalbard mass balance of -39 cm w.e. yr^{-1}, which corresponds to a eustatic sea level rise of 0.037 mm yr^{-1}.
- There is large interannual variability in B_{clim}, which is controlled by summer melt. Decreasing B_{clim} over the study period is primarily due to increased summer temperatures, amplified by the albedo feedback.
- Refreezing plays a major role in Svalbard B_{clim}, representing about a quarter of annual accumulation. With increasing air temperatures over the study period, refreezing and water retention decrease both in absolute amounts and relative percentage of total accumulation
- With increasing ELAs, firn extent is reduced and subsurface cooling occurs in the vicinity of the ELA, while subsurface warming occurs in the lower ablation area. Increased run-off and changes in the hydrological and thermal regimes are likely to be important for glacier flow.
- Sensitivity experiments suggest that the expected future precipitation increase cannot compensate for the expected rise in air temperatures. Perturbing temperature by 6 K and precipitation by 30 % (north-eastern Svalbard) and by 4 K and 5 % (western Svalbard) as projected for 2100 from a regional climate model (Førland et al., 2011), results in modelled ELA above the summits of most of today's ice caps and ice fields.

Two major shortcomings in the meteorological forcing are identified. First, prior to 1980, temperatures and precipitation are too low. This may be caused by an inaccurate representation of sea ice in the reanalysis data for the pre-satellite period. Second, the downscaling methodology likely introduces biases where the surface type (ocean, sea ice, tundra, glacier) does not match across the scale gap between the coarsely resolved reanalysis and our finer grid resolution. This latter problem may be overcome by using the same downscaling approach on 10–25 km RCM output instead of the ERA-40 and ERA-Interim data, which could potentially improve our results.

In addition to considerable mass change, this study suggests there are significant changes in the thermal and hydrological regimes of Svalbard glaciers, which in turn may have important implications for glacier dynamics, as suggested by recent observation of ice cap destabilization (Dunse et al., 2015); an understudied process that requires further investigation.

8 Data availability

ERA-40 and ERA-Interim data were retrieved from the ECMWF Public Datasets web interface at http://apps.ecmwf.int/datasets/.

The DEBAM code is available at https://github.com/regine/meltmodel, and a user manual is retrieved from http://www.lygi.me/meltmodel/.

MODIS surface Albedo (MOD10A1/MYD10A1) was downloaded from url: ftp://n5eil01u.ecs.nsidc.org/SAN/ and MODIS surface temperatures (MOD11A1/MYD11A1) from http://e4ftl01.cr.usgs.gov/MODIS_Dailies_E/.

We are grateful to J. Vrugt for sharing the DREAM code and defining the likelihood function.

Weather station data are provided by the Norwegian meteorological office and are available through http://eklima.met.no, and by the University Centre of Svalbard through http://www.unis.no/resources/weather-stations/.

Radiation from the BRSN-station in Ny-Ålesund are provided by Maturilli et al. (2014).

C. Nuth provided glacier outlines and digital elevation models, which he made available at http://www.glims.org/RGI/rgi50_files/07_rgi50_Svalbard.zip.

Glacier-wide mass balances are available from the World Glacier Monitoring Service http://wgms.ch/latest-glacier-mass-balance-data/ but individual point measurements were contributed by the responsible researchers. Mass balances from Hornsund were provided by B. Luks and from Nordenskiöldbreen by V. Pohjola and W. van Pelt. A publication describing the downscaled forcing data set in more detail, along with a publication for a data repository, is currently in progress.

The Supplement related to this article is available online at doi:10.5194/tc-11-191-2017-supplement.

Acknowledgements. The Norwegian Ministry of Education funded a scholarship for T. Østby. Fieldwork and analysis have been funded by ESA (CRYOVEX), NFR TIGRIF, EU Ice2Sea, NFR CRYOMET and the NCoE SVALI. The authors gratefully acknowledge the enthusiastic support of T. Dunse, T. Eiken, G. Moholdt and the Austfonna team during fieldwork.

Edited by: G. H. Gudmundsson
Reviewed by: X. Fettweis and one anonymous referee

References

Aas, K. S., Dunse, T., Collier, E., Schuler, T. V., Berntsen, T. K., Kohler, J., and Luks, B.: The climatic mass balance of Svalbard glaciers: a 10-year simulation with a coupled atmosphere-glacier mass balance model, The Cryosphere, 10, 1089–1104, doi:10.5194/tc-10-1089-2016, 2016.

Ackerman, S., Strabala, K., Menzel, W., Frey, R., Moeller, C., and Gumley, L.: Discriminating clear sky from clouds with MODIS, J. Geophys. Res.-Atmos., 103, 32141–32157, doi:10.1029/1998JD200032, 1998.

Aleksandrov, Y., Bryazgin, N., Forland, E., Radionov, V., and Svyashchennikov, P.: Seasonal, interannual and long-term variability of precipitation and snow depth in the region of the Barents and Kara seas, Polar Res., 24, 69–85, doi:10.1111/j.1751-8369.2005.tb00141.x, 2005.

AMAP: Snow, Water, Ice and Permafrost in the Arctic (SWIPA): Climate Change and the Cryosphere, Arctic Monitoring and Assessment Programme (AMAP), Oslo, Norway, XII + 538 pp., 2011.

Andreas, E.: A theory for the scalar roughness and the scalar transfer coefficients over snow and sea ice, Bound.-Lay. Meteorol., 38, 159–184, 1987.

Arendt, A.: Approaches to modelling the surface albedo of a high Arctic glacier, Geogr. Ann. A, 81, 477–487, 1999.

Arendt, A., Bliss, A., Bolch, T., Cogley, J. G., Gardner, A. S., Hagen, J.-O., Hock, R., Huss, M., Kaser, G., Kienholz, C., Pfeffer, W. T., Moholdt, G., Paul, F., Radić, V., Andreassen, L., Bajracharya, S., Barrand, N. E., Beedle, M., Berthier, E., Bhambri, R., Brown, I., Burgess, E., Burgess, D., Cawkwell, F., Chinn, T., Copland, L., Davies, B., De Angelis, H., Dolgova, E., Earl, L., Filbert, K., Forester, R., Fountain, A. G., Frey, H., Giffen, B., Glasser, N., Guo, W. Q., Gurney, S., Hagg, W., Hall, D., Haritashya, U. K., Hartmann, G., Helm, C., Herreid, S., Howat, I., Kapustin, G., Khromova, T., König, M., Kohler, J., Kriegel, D., Kutuzov, S., Lavrentiev, I., LeBris, R., Liu, S. Y., Lund, J., Manley, W., Marti, R., Mayer, C., Miles, E. S., Li, X., Menounos, B., Mercer, A., Mölg, N., Mool, P., Nosenko, G., Negrete, A., Nuimura, T., Nuth, C., Pettersson, R., Racoviteanu, A., Ranzi, R., Rastner, P., Rau, F., Raup, B., Rich, J., Rott, H., Sakai, A., Schneider, C., Seliverstov, Y., Sharp, M., Sigurdsson, O., Stokes, C., Way, R. G., Wheate, R., Winsvold, S., Wolken, G., Wyatt, F., and Zheltyhina, N.: Randolph Glacier Inventory – A Dataset of Global Glacier Outlines: Version 5.0, Global Land Ice Measurements from Space, Boulder Colorado, USA, 2015.

Arnold, N., Rees, W., Hodson, A., and Kohler, J.: Topographic controls on the surface energy balance of a high Arctic valley glacier, J. Geophys. Res.-Earth, 111, F02011, doi:10.1029/2005JF000426, 2006.

Barstad, I. and Smith, R.: Evaluation of an orographic precipitation model, J. Hydrometeorol., 6, 85–99, doi:10.1175/JHM-404.1, 2005.

Björnsson, H., Gjessing, Y., Hamran, S.-E., Hagen, J., Liestøl, O., Pálsson, F., and Erlingsson, B.: The thermal regime of subpolar glaciers mapped by multi-frequency radio-echo sounding, J. Glaciol., 42, 23–32, 1996.

Błaszczyk, M., Jania, J. A., and Hagen, J. O.: Tidewater glaciers of Svalbard: Recent changes and estimates of calving fluxes, Pol. Polar Res., 30, 85–142, 2009.

Bogren, W. S., Burkhart, J. F., and Kylling, A.: Tilt error in cryospheric surface radiation measurements at high latitudes: a model study, The Cryosphere, 10, 613–622, doi:10.5194/tc-10-613-2016, 2016.

Bougamont, M. and Bamber, J.: A surface mass balance model for the Greenland ice sheet, J. Geophys. Res.-Earth, 110, F04018, doi:10.1029/2005JF000348, 2005.

Bromwich, D. H. and Fogt, R. L.: Strong Trends in the Skill of the ERA-40 and NCEP–NCAR Reanalyses in the High and Midlatitudes of the Southern Hemisphere, 1958–2001, J. Climate, 17, 4603–4619, doi:10.1175/3241.1, 2004.

Charalampidis, C., van As, D., Box, J. E., van den Broeke, M. R., Colgan, W. T., Doyle, S. H., Hubbard, A. L., MacFerrin, M., Machguth, H., and Smeets, C. J. P. P.: Changing surface-atmosphere energy exchange and refreezing capacity of the lower accumulation area, West Greenland, The Cryosphere, 9, 2163–2181, doi:10.5194/tc-9-2163-2015, 2015.

Church, J., White, N., Konikow, L., Domingues, C., Cogley, J., Rignot, E., Gregory, J., van den Broeke, M., Monaghan, A., and Velicogna, I.: Revisiting the Earth's sea-level and energy budgets from 1961 to 2008, Geophys. Res. Lett., 38, L18601, doi:10.1029/2011GL048794, 2011.

Claremar, B., Obleitner, F., Reijmer, C., Pohjola, V., Waxegard, A., Karner, F., and Rutgersson, A.: Applying a Mesoscale Atmospheric Model to Svalbard Glaciers, Adv. Meteorol., 2012, 321649, doi:10.1155/2012/321649, 2012.

Cogley, J., Hock, R., Rasmussen, L., Arendt, A., Bauder, A., Braithwaite, R., Jansson, P., Kaser, G., Müller, M., Nicholson, L., and Zemp, M.: Glossary of glacier mass balance and related terms, Tech. rep., UNESCO-IHP, 2011.

Cox, C., Humphrey, N., and Harper, J.: Quantifying meltwater refreezing along a transect of sites on the Greenland ice sheet, The Cryosphere, 9, 691–701, doi:10.5194/tc-9-691-2015, 2015.

Crochet, P., Jóhannesson, T., Jónsson, T., Sigurdsson, O., Björnsson, H., Pálsson, F., and Barstad, I.: Estimating the spatial distribution of precipitation in Iceland using a linear model of orographic precipitation, J. Hydrometeorol., 8, 1285–1306, doi:10.1175/2007JHM795.1, 2007.

De Woul, M. and Hock, R.: Static mass-balance sensitivity of Arctic glaciers and ice caps using a degree-day approach, Ann. Glaciol., 42, 217–224, doi:10.3189/172756405781813096, 2005.

Dee, D. P., Uppala, S. M., Simmons, A. J., Berrisford, P., Poli, P., Kobayashi, S., Andrae, U., Balmaseda, M. A., Balsamo, G., Bauer, P., Bechtold, P., Beljaars, A. C. M., van de Berg, L., Bidlot, J., Bormann, N., Delsol, C., Dragani, R., Fuentes, M., Geer, A. J., Haimberger, L., Healy, S. B., Hersbach, H., Hólm, E. V., Isaksen, L., Kållberg, P., Köhler, M., Matricardi, M., McNally, A. P., Monge-Sanz, B. M., Morcrette, J.-J., Park, B.-K., Peubey, C., de Rosnay, P., Tavolato, C., Thépaut, J.-N., and Vitart, F.: The ERA-Interim reanalysis: configuration and performance of the data assimilation system, Q. J. Roy. Meteor. Soc., 137, 553–597, doi:10.1002/qj.828, 2011.

Douville, H., Royer, J.-F., and Mahfouf, J.-F.: A new snow parameterization for the Meteo-France climate model, Part I: Validation in stand alone experiment, Clim. Dynam., 12, 21–35, 1995.

Dunse, T., Schellenberger, T., Hagen, J. O., Kääb, A., Schuler, T. V., and Reijmer, C. H.: Glacier-surge mechanisms promoted by a hydro-thermodynamic feedback to summer melt, The Cryosphere, 9, 197–215, doi:10.5194/tc-9-197-2015, 2015.

Elsberg, D., Harrison, W., Echelmeyer, K., and Krimmel, R.: Quantifying the effects of climate and surface change on glacier mass balance, J. Glaciol., 47, 649–658, doi:10.3189/172756501781831783, 2001.

Fiddes, J. and Gruber, S.: TopoSCALE v.1.0: downscaling gridded climate data in complex terrain, Geosci. Model Dev., 7, 387–405, doi:10.5194/gmd-7-387-2014, 2014.

Førland, E. J. and Hanssen-Bauer, I.: Increased Precipitation in the Norwegian Arctic: True or False?, Clim. Change, 46, 485–509, doi:10.1023/A:1005613304674, 2000.

Førland, E. and Hanssen-Bauer, I.: Past and future climate variations in the Norwegian Arctic: overview and novel analyses, Polar Res., 22, 113–124, doi:10.1111/j.1751-8369.2003.tb00102.x, 2003.

Førland, E., Hanssen-Bauer, I., and Nordli, Ø.: Climate statistics and long-term series of temperature and precipitation at Svalbard and Jan Mayen, Klima, 27, dNMI report, Norwegian Meteorological Institute, Oslo, 1997.

Førland, E. J., Benestad, R., Hanssen-Bauer, I., Haugen, J., and Skaugen, T.: Temperature and Precipitation Development at Svalbard 1900–2100, Adv. Meteorol., 2011, 893790, doi:10.1155/2011/893790, 2011.

Frey, R. A., Ackerman, S. A., Liu, Y., Strabala, K. I., Zhang, H., Key, J. R., and Wang, X.: Cloud detection with MODIS. Part I: Improvements in the MODIS cloud mask for collection 5, J. Atmos. Ocean. Tech., 25, 1057–1072, doi:10.1175/2008JTECHA1052.1, 2008.

Gardner, A. and Sharp, M.: A review of snow and ice albedo and the development of a new physically based broadband albedo parameterization, J. Geophys. Res.-Earth, 115, F01009, doi:10.1029/2009JF001444, 2010.

Gardner, A. S., Moholdt, G., Cogley, J. G., Wouters, B., Arendt, A. A., Wahr, J., Berthier, E., Hock, R., Pfeffer, W. T., Kaser, G., Ligtenberg, S. R. M., Bolch, T., Sharp, M. J., Hagen, J. O., van den Broeke, M. R., and Paul, F.: A Reconciled Estimate of Glacier Contributions to Sea Level Rise: 2003 to 2009, Science, 340, 852–857, doi:10.1126/science.1234532, 2013.

Giesen, R. H. and Oerlemans, J.: Climate-model induced differences in the 21st century global and regional glacier contributions to sea-level rise, Clim. Dynam., 41, 3283–3300, doi:10.1007/s00382-013-1743-7, 2013.

Grabiec, M., Leszkiewicz, J., Głowacki, P., and Jania, J.: Distribution of snow accumulation on some glaciers of Spitsbergen, Pol. Polar Res., 27, 309–326, 2006.

Grabiec, M., Jania, J. A., Puczko, D., Kolondra, L., and Budzik, T.: Surface and bed morphology of Hansbreen, a tidewater glacier in Spitsbergen, Pol. Polar Res., 33, 111–138, doi:10.2478/v10183-012-0010-7, 2012.

Greuell, W. and Konzelmann, T.: Numerical modeling of the energy-balance and the englacial temperature of the Greenland ice-sheet – calculations for the eth-camp location (West Greenland, 1155m asl), Global Planet. Change, 9, 91–114, 1994.

Greuell, W., Kohler, J., Obleitner, F., Glowacki, P., Melvold, K., Bernsen, E., and Oerlemans, J.: Assessment of interannual variations in the surface mass balance of 18 Svalbard glaciers from the Moderate Resolution Imaging Spectroradiometer/Terra albedo product, J. Geophys. Res.-Atmos., 112, D07105, doi:10.1029/2006JD007245, 2007.

Hagen, J., Kohler, J., Melvold, K., and Winther, J.: Glaciers in Svalbard: mass balance, runoff and freshwater flux, Polar Res., 22, 145–159, 2003a.

Hagen, J., Melvold, K., Pinglot, F., and Dowdeswell, J.: On the Net Mass Balance of the Glaciers and Ice Caps in Svalbard, Norwegian Arctic, Arct. Antarct. Alp. Res., 35, 264–270, 2003b.

Hall, D., Key, J., Casey, K., Riggs, G., and Cavalieri, D.: Sea ice surface temperature product from MODIS, IEEE T. Geosci. Remote, 42, 1076–1087, doi:10.1109/TGRS.2004.825587, 2004.

Hall, D. K. and Riggs, G. A.: Accuracy assessment of the MODIS snow products, Hydrol. Process., 21, 1534–1547, doi:10.1002/hyp.6715, 2007.

Hall, D. K., Box, J. E., Casey, K. A., Hook, S. J., Shuman, C. A., and Steffen, K.: Comparison of satellite-derived and in-situ observations of ice and snow surface temperatures over Greenland, Remote Sens. Environ., 112, 3739–3749, doi:10.1016/j.rse.2008.05.007, 2008.

Hansen, B. B., Isaksen, K., Benestad, R. E., Kohler, J., Pedersen, Å. Ø., Loe, L. E., Coulson, S. J., Larsen, J. O., and Øystein Varpe: Warmer and wetter winters: characteristics and implications of an extreme weather event in the High Arctic, Environ. Res. Lett., 9, 114021, doi:10.1088/1748-9326/9/11/114021, 2014.

Hanssen-Bauer, I. and Førland, E. J.: Long-term trends in precipitation and temperature in the Norwegian Arctic: can they be explained by changes in atmospheric circulation patterns?, Clim. Res., 110, 143–153, 1998.

Harper, J., Humphrey, N., Pfeffer, W. T., Brown, J., and Fettweis, X.: Greenland ice-sheet contribution to sea-level rise buffered by meltwater storage in firn, Nature, 491, 240–243, doi:10.1038/nature11566, 2012.

Herron, M. and Langway, J. C.: Firn densification: an empirical model, J. Glaciol., 25, 373–385, 1980.

Hisdal, V.: Svalbard, Nature and History, Vol. 12, Norsk polarinstitutt, 1998.

Hock, R. and Holmgren, B.: A distributed surface energy-balance model for complex topography and its application to Storglaciaren, Sweden, J. Glaciol., 51, 25–36, 2005.

Huss, M.: Extrapolating glacier mass balance to the mountain-range scale: the European Alps 1900–2100, The Cryosphere, 6, 713–727, doi:10.5194/tc-6-713-2012, 2012.

Huss, M. and Farinotti, D.: Distributed ice thickness and volume of all glaciers around the globe, J. Geophys. Res.-Earth, 117, F04010, doi:10.1029/2012JF002523, 2012.

Huss, M., Bauder, A., and Funk, M.: Homogenization of long-term mass-balance time series, Ann. Glaciol., 50, 198–206, doi:10.3189/172756409787769627, 2009.

IPCC: Climate Change 2013: The Physical Science Basis, Contribution of Working Group I to the Fifth Assessment Report of the Intergovernmental Panel on Climate Change, Cambridge University Press, Cambridge, UK, New York, NY, USA, doi:10.1017/CBO9781107415324, 2013.

Irvine-Fynn, T. D. L., Hodson, A. J., Moorman, B. J., Vatne, G., and Hubbard, A. L.: Polythermal Glacier Hydrology: a Review, Rev. Geophys., 49, RG4002, doi:10.1029/2010RG000350, 2011.

Jacob, T., Wahr, J., Pfeffer, W. T., and Swenson, S.: Recent contributions of glaciers and ice caps to sea level rise, Nature, 482, 514–518, 2012.

James, T. D., Murray, T., Barrand, N. E., Sykes, H. J., Fox, A. J., and King, M. A.: Observations of enhanced thinning in the upper reaches of Svalbard glaciers, The Cryosphere, 6, 1369–1381, doi:10.5194/tc-6-1369-2012, 2012.

Kääb, A., Lefauconnier, B., and Melvold, K.: Flow field of Kronebreen, Svalbard, using repeated Landsat 7 and ASTER data, Ann. Glaciol., 42, 7–13, doi:10.3189/172756405781812916, 2005.

Kaesmacher, O. and Schneider, C.: An objective circulation pattern classification for the region of Svalbard, Geogr. Ann. A, 93, 259–271, doi:10.1111/j.1468-0459.2011.00431.x, 2011.

Kohler, J., James, T. D., Murray, T., Nuth, C., Brandt, O., Barrand, N. E., Aas, H. F., and Luckman, A.: Acceleration in thinning rate on western Svalbard glaciers, Geophys. Res. Lett., 34, L18502, doi:10.1029/2007GL030681, 2007.

Kumar, L., Skidmore, A., and Knowles, E.: Modelling topographic variation in solar radiation in a GIS environment, Int. J. Geogr. Inf. Sci., 11, 475–497, doi:10.1080/136588197242266, 1997.

Laloy, E. and Vrugt, J. A.: High-dimensional posterior exploration of hydrologic models using multiple-try DREAM(ZS) and high-performance computing, Water Resour. Res., 48, W01526, doi:10.1029/2011WR010608, 2012.

Lang, C., Fettweis, X., and Erpicum, M.: Stable climate and surface mass balance in Svalbard over 1979–2013 despite the Arctic warming, The Cryosphere, 9, 83–101, doi:10.5194/tc-9-83-2015, 2015a.

Lang, C., Fettweis, X., and Erpicum, M.: Future climate and surface mass balance of Svalbard glaciers in an RCP8.5 climate scenario: a study with the regional climate model MAR forced by MIROC5, The Cryosphere, 9, 945–956, doi:10.5194/tc-9-945-2015, 2015b.

Loeng, H.: Features of the physical oceanographic conditions of the Barents Sea, Polar Res., 10, 5–18, 1991.

Machguth, H., MacFerrin, M., van As, D., Box, J. E., Charalampidis, C., Colgan, W., Fausto, R. S., Meijer, H. A., Mosley-Thompson, E., and van de Wal, R. S.: Greenland meltwater storage in firn limited by near-surface ice formation, Nat. Clim. Change, 6, 390–393, doi:10.1038/nclimate2899, 2016.

Martín-Español, A., Navarro, F., Otero, J., Lapazaran, J., and Błaszczyk, M.: Estimate of the total volume of Svalbard glaciers, and their potential contribution to sea-level rise, using new regionally based scaling relationships, J. Glaciol., 61, 29–41, doi:10.3189/2015JoG14J159, 2015.

Marzeion, B., Jarosch, A. H., and Hofer, M.: Past and future sea-level change from the surface mass balance of glaciers, The Cryosphere, 6, 1295–1322, doi:10.5194/tc-6-1295-2012, 2012.

Maturilli, M., Herber, A., and König-Langlo, G.: Climatology and time series of surface meteorology in Ny-Ålesund, Svalbard, Earth Syst. Sci. Data, 5, 155–163, doi:10.5194/essd-5-155-2013, 2013.

Maturilli, M., Herber, A., and König-Langlo, G.: Basic and other measurements of radiation from the Baseline Surface Radiation Network (BSRN) Station Ny-Ålesund in the years 1992 to 2013, reference list of 253 datasets, doi:10.1594/PANGAEA.150000, 2014.

Meier, M. F., Dyurgerov, M. B., Rick, U. K., O'Neel, S., Pfeffer, W. T., Anderson, R. S., Anderson, S. P., and Glazovsky, A. F.: Glaciers dominate Eustatic sea-level rise in the 21st century, Science, 317, 1064–1067, 2007.

Mèmin, A., Rogister, Y., Hinderer, J., Omang, O. C., and Luck, B.: Secular gravity variation at Svalbard (Norway) from ground observations and GRACE satellite data, Geophys. J. Int., 184, 1119–1130, doi:10.1111/j.1365-246X.2010.04922.x, 2011.

Michel, D., Philipona, R., Ruckstuhl, C., Vogt, R., and Vuilleumier, L.: Performance and uncertainty of CNR1 net radiometers during a one-year field comparison, J. Atmos. Ocean. Tech., 25, 442–451, doi:10.1175/2007JTECHA973.1, 2008.

Mikkelsen, A. B., Hubbard, A., MacFerrin, M., Box, J. E., Doyle, S. H., Fitzpatrick, A., Hasholt, B., Bailey, H. L., Lindbäck, K., and Pettersson, R.: Extraordinary runoff from the Greenland ice sheet in 2012 amplified by hypsometry and depleted firn retention, The Cryosphere, 10, 1147–1159, doi:10.5194/tc-10-1147-2016, 2016.

Moholdt, G., Nuth, C., Hagen, J., and Kohler, J.: Recent elevation changes of Svalbard glaciers derived from ICESat laser altimetry, Remote Sens. Environ., 114, 2756–2767, 2010.

Möller, M., Obleitner, F., Reijmer, C. H., Pohjola, V. A., Głowacki, P., and Kohler, J.: Adjustment of regional climate model output for modeling the climatic mass balance of all glaciers on Svalbard, J. Geophys. Res.-Atmos., 121, 5411–5429, doi:10.1002/2015JD024380, 2016.

Murray, T., Stuart, G. W., Miller, P. J., Woodward, J., Smith, A. M., Porter, P. R., and Jiskoot, H.: Glacier surge propagation by thermal evolution at the bed, J. Geophys. Res.-Sol. Ea., 105, 13491–13507, doi:10.1029/2000JB900066, 2000.

Nordli, O., Przybylak, R., Ogilvie, A. E. J., and Isaksen, K.: Longterm temperature trends and variability on Spitsbergen: the extended Svalbard Airport temperature series, 1898–2012, Polar Res., 33, 21349, doi:10.3402/polar.v33.21349, 2014.

Nuth, C., Moholdt, G., Kohler, J., Hagen, J. O., and Kääb, A.: Svalbard glacier elevation changes and contribution to sea level rise, J. Geophys. Res., 115, F01008, doi:10.1029/2008JF001223, 2010.

Nuth, C., Moholdt, G., Kohler, J., Hagen, J., and Kääb, A.: Svalbard glacier elevation changes and contribution to sea level rise, J. Geophys. Res.-Earth, 115, F01008, doi:10.1029/2008JF001223, 2010.

Nuth, C., Kohler, J., König, M., von Deschwanden, A., Hagen, J. O., Kääb, A., Moholdt, G., and Pettersson, R.: Decadal changes from a multi-temporal glacier inventory of Svalbard, The Cryosphere, 7, 1603–1621, doi:10.5194/tc-7-1603-2013, 2013.

Nuth, C., Schuler, T. V., Kohler, J., Altena, B., and Hagen, J. O.: Estimating the long-term calving flux of Kronebreen, Svalbard, from geodetic elevation changes and mass-balance modelling, J. Glaciol., 58, 119–133, doi:10.3189/2012JoG11J036, 2012.

Oerlemans, J. and Knap, W.: A 1 year record of global radiation and albedo in the ablation zone of Morteratschgletscher, Switzerland, J. Glaciol., 44, 231–238, 1998.

Østby, T. I., Schuler, T. V., Hagen, J. O., Hock, R., and Reijmer, L. H.: Parameter uncertainty, refreezing and surface energy balance modelling at Austfonna ice cap, Svalbard, 2004–08, Ann. Glaciol., 54, 229–240, doi:10.3189/2013AoG63A280, 2013.

Østby, T. I., Schuler, T. V., and Westermann, S.: Severe cloud contamination of MODIS Land Surface Temperatures over an Arctic ice cap, Svalbard, Remote Sens. Environ., 142, 95–102, doi:10.1016/j.rse.2013.11.005, 2014.

Phillips, T., Rajaram, H., and Steffen, K.: Cryo-hydrologic warming: A potential mechanism for rapid thermal response of ice sheets, Geophys. Res. Lett., 37, L20503, doi:10.1029/2010GL044397, 2010.

Pinglot, J., Pourchet, M., Lefauconnier, B., Hagen, J., Isaksson, E., Vaikmae, R., and Kamiyama, K.: Accumulation in Svalbard glaciers deduced from ice cores with nuclear tests and Chernobyl reference layers, Polar Res., 18, 315–321, doi:10.1111/j.1751-8369.1999.tb00309.x, 1999.

Pinglot, J. F., Hagen, J. O., Melvold, K., Eiken, T., and Vincent, C.: A mean net accumulation pattern derived from radioactive layers and radar soundings on Austfonna, Nordaustlandet, Svalbard, J. Glaciol., 47, 555–566, 2001.

Pohjola, V., Martma, T., Meijer, H., Moore, J., Isaksson, E., Vaikmae, R., and Van de Wal, R.: Reconstruction of three centuries of annual accumulation rates based on the record of stable isotopes of water from Lomonosovfonna, Svalbard, Ann. Glaciol., 35, 57–62, doi:10.3189/172756402781816753, 2002.

Radić, V. and Hock, R.: Regional and global volumes of glaciers derived from statistical upscaling of glacier inventory data, J. Geophys. Res.-Earth, 115, F01010, doi:10.1029/2009JF001373, 2010.

Radić, V., Bliss, A., Beedlow, A. C., Hock, R., Miles, E., and Cogley, J. G.: Regional and global projections of twenty-first century glacier mass changes in response to climate scenarios from global climate models, Clim. Dynam., 42, 37–58, doi:10.1007/s00382-013-1719-7, 2014.

Ratti, C.: Urban analysis for environmental prediction, PhD thesis, University of Cambridge Department of Architecture, 2001.

Reda, I. and Andreas, A.: Solar position algorithm for solar radiation applications, Sol. Energy, 76, 577–589, doi:10.1016/j.solener.2003.12.003, 2004.

Reijmer, C. H. and Hock, R.: Internal accumulation on Storglaciidren, Sweden, in a multi-layer snow model coupled to a distributed energy- and mass-balance model, J. Glaciol., 54, 61–72, 2008.

Reijmer, C. H., van den Broeke, M. R., Fettweis, X., Ettema, J., and Stap, L. B.: Refreezing on the Greenland ice sheet: a comparison of parameterizations, The Cryosphere, 6, 743–762, doi:10.5194/tc-6-743-2012, 2012.

Rodrigues, J.: The rapid decline of the sea ice in the Russian Arctic, Cold Reg. Sci. Technol., 54, 124–142, doi:10.1016/j.coldregions.2008.03.008, 2008.

Rogers, J., Yang, L., and Li, L.: The role of Fram Strait winter cyclones on sea ice flux and on Spitsbergen air temperatures, Geophys. Res. Lett., 32, L06709, doi:10.1029/2004GL022262, 2005.

Sand, K., Winther, J., Marechal, D., Bruland, O., and Melvold, K.: Regional variations of snow accumulation on Spitsbergen, Svalbard, 1997–99, Nord. Hydrol., 34, 17–32, 2003.

Scambos, T. A., Haran, T. M., and Massom, R.: Validation of AVHRR and MODIS ice surface temperature products using in situ radiometers, Ann. Glaciol., 44, 345–351, doi:10.3189/172756406781811457, 2006.

Schaaf, C. B., Wang, Z., and Strahler, A. H.: Commentary on Wang and Zender-MODIS snow albedo bias at high solar zenith angles relative to theory and to in situ observations in Greenland, Remote Sens. Environ., 115, 1296–1300, doi:10.1016/j.rse.2011.01.002, 2011.

Schneider, T. and Jansson, P.: Internal accumulation in firn and its significance for the mass balance of Storglaciaren, Sweden, J. Glaciol., 50, 25–34, 2004.

Schuler, T. V., Crochet, P., Hock, R., Jackson, M., Barstad, I., and Johannesson, T.: Distribution of snow accumulation on the Svartisen ice cap, Norway, assessed by a model of orographic precipitation, Hydrol. Proc., 22, 3998–4008, 2008.

Schuler, T. V., Dunse, T., Østby, T. I., and Hagen, J. O.: Meteorological conditions on an Arctic ice cap – 8 years of automatic weather station data from Austfonna, Svalbard, Int. J. Climatol., 34, 2047–2058, doi:10.1002/joc.3821, 2014.

Screen, J. A. and Simmonds, I.: Erroneous Arctic Temperature Trends in the ERA-40 Reanalysis: A Closer Look, J. Climate, 24, 2620–2627, doi:10.1175/2010JCLI4054.1, 2011.

Serreze, M. C. and Francis, J. A.: The arctic amplification debate, Clim. Change, 76, 241–264, doi:10.1007/s10584-005-9017-y, 2006.

Smith, R. B. and Barstad, I.: A linear theory of orographic precipitation, J. Atmos. Sci., 61, 1377–1391, 2004.

Uppala, S. M., Kållberg, P. W., Simmons, A. J., Andrae, U., Bechtold, V. D. C., Fiorino, M., Gibson, J. K., Haseler, J., Hernandez, A., Kelly, G. A., Li, X., Onogi, K., Saarinen, S., Sokka, N., Allan, R. P., Andersson, E., Arpe, K., Balmaseda, M. A., Beljaars, A. C. M., Berg, L. V. D., Bidlot, J., Bormann, N., Caires, S., Chevallier, F., Dethof, A., Dragosavac, M., Fisher, M., Fuentes, M., Hagemann, S., Hólm, E., Hoskins, B. J., Isaksen, L., Janssen, P. A. E. M., Jenne, R., McNally, A. P., Mahfouf, J.-F., Morcrette, J.-J., Rayner, N. A., Saunders, R. W., Simon, P., Sterl, A., Trenberth, K. E., Untch, A., Vasiljevic, D., Viterbo, P., and Woollen, J.: The ERA-40 re-analysis, Q. J. Roy. Meteor. Soc., 131, 2961–3012, doi:10.1256/qj.04.176, 2005.

van Pelt, W. and Kohler, J.: Modelling the long-term mass balance and firn evolution of glaciers around Kongsfjorden, Svalbard, J. Glaciol., 61, 731–744, doi:10.3189/2015JoG14J223, 2015.

van Pelt, W. J. J., Oerlemans, J., Reijmer, C. H., Pohjola, V. A., Pettersson, R., and van Angelen, J. H.: Simulating melt, runoff and refreezing on Nordenskiöldbreen, Svalbard, using a coupled snow and energy balance model, The Cryosphere, 6, 641–659, doi:10.5194/tc-6-641-2012, 2012.

van Pelt, W. J. J., Kohler, J., Liston, G. E., Hagen, J. O., Luks, B., Reijmer, C. H., and Pohjola, V. A.: Multidecadal climate and seasonal snow conditions in Svalbard, J. Geophys. Res.-Earth, 121, 2100–2117, doi:10.1002/2016JF003999, 2016.

Vaughan, D. G., Comiso, J. C., Allison, I., Carrasco, J., Kaser, G., Kwok, R., Mote, P., Murray, T., Paul, F., Ren, J., Rignot, E., Solomina, O., Steffen, K., and Zhang, T.: Observations: Cryosphere, in: Climate Change 2013: The Physical Science Basis. Contribution of Working Group I to the Fifth Assessment Report of the Intergovernmental Panel on Climate Change, edited by: Stocker, T. F., Qin, D., Plattner, G. K., Tignor, M., Allen, S. K., Boschung, J., Nauels, A., Xia, Y., Bex, V., and Midgley, P. M., Cambridge University Press, 4, 317–382, 2013.

Vrugt, J. A., ter Braak, C. J. F., Diks, C. G. H., Robinson, B. A., Hyman, J. M., and Higdon, D.: Accelerating Markov Chain Monte Carlo Simulation by Differential Evolution with Self-Adaptive Randomized Subspace Sampling, Int. J. Nonlin. Sci. Num., 10, 273–290, 2009.

Walczowski, W. and Piechura, J.: Influence of the West Spitsbergen Current on the local climate, Int. J. Climatol., 31, 1088–1093, doi:10.1002/joc.2338, 2011.

Wan, Z.: New refinements and validation of the MODIS Land-Surface Temperature/Emissivity products, Remote Sens. Environ., 112, 59–74, doi:10.1016/j.rse.2006.06.026, 2008.

Wan, Z.: New refinements and validation of the collection-6 {MODIS} land-surface temperature/emissivity product, Remote Sens. Environ., 140, 36–45, doi:10.1016/j.rse.2013.08.027, 2014.

Wan, Z. and Dozier, J.: A generalized split-window algorithm for retrieving land-surface temperature from space, IEEE T. Geosci. Remote, 34, 892–905, 1996.

Wientjes, I. G. M., Van de Wal, R. S. W., Reichart, G. J., Sluijs, A., and Oerlemans, J.: Dust from the dark region in the western ablation zone of the Greenland ice sheet, The Cryosphere, 5, 589–601, doi:10.5194/tc-5-589-2011, 2011.

Wilson, N. J. and Flowers, G. E.: Environmental controls on the thermal structure of alpine glaciers, The Cryosphere, 7, 167–182, doi:10.5194/tc-7-167-2013, 2013.

Winther, J., Bruland, O., Sand, K., Gerland, S., Marechal, D., Ivanov, B., Glowacki, P., and Konig, M.: Snow research in Svalbard – an overview, Polar Res., 22, 125–144, doi:10.1111/j.1751-8369.2003.tb00103.x, 2003.

Wright, A., Wadham, J., Siegert, M., Luckman, A., and Kohler, J.: Modelling the impact of superimposed ice on the mass balance of an Arctic glacier under scenarios of future climate change, Ann. Glaciol., 42, 277—283, 2005.

Zemp, M., Thibert, E., Huss, M., Stumm, D., Rolstad Denby, C., Nuth, C., Nussbaumer, S. U., Moholdt, G., Mercer, A., Mayer, C., Joerg, P. C., Jansson, P., Hynek, B., Fischer, A., Escher-Vetter, H., Elvehøy, H., and Andreassen, L. M.: Reanalysing glacier mass balance measurement series, The Cryosphere, 7, 1227–1245, doi:10.5194/tc-7-1227-2013, 2013.

Zevenbergen, L. and Thorne, C.: Quantitative-analysis of land surface-topography, Earth Surf. Proc. Land., 12, 47–56, doi:10.1002/esp.3290120107, 1987.

Zuo, Z. and Oerlemans, J.: Modelling albedo and specific balance of the Greenland ice sheet: Calculations for the Sondre Stromfjord transect, J. Glaciol., 42, 305–317, 1996.